Maturation of Hippocampus-Medial Prefrontal Cortex Projections Defines a Pathway-Specific Sensitive Period for Cognitive Flexibility

Arely Cruz-Sanchez[1,2], Anusha Abdusalom[1], Helen Chasiotis[1], Radu Gugustea[1], Unza Mumtaz[1], Maryam Hasantash[3], Christoph Anacker[3] and Maithe Arruda-Carvalho[1,2†]

[1] University of Toronto Scarborough, Department of Psychology, Toronto, Ontario, Canada, M1C1A4

[2] University of Toronto Scarborough, Department of Cell and Systems Biology, Toronto, Ontario, Canada, M1C1A4

[3]Department of Psychiatry, Columbia University, and Research Foundation for Mental Hygiene, Inc. (RFMH), New York State Psychiatric Institute (NYSPI), New York, NY, 10032, USA

[†]Correspondence should be addressed to:

Maithe Arruda-Carvalho
University of Toronto Scarborough, Department of Psychology
1265 Military Trail, Science Wing, Room SW533, Toronto, ON, M1C 1A4, Canada
m.arrudacarvalho@utoronto.ca
@ArruCarval_lab

Summary (150 words)

The septotemporal axis of the hippocampus separates it into domains with unique molecular, cellular, downstream connectivity and behavioral profiles, and yet very little is known about the ontogenesis of these highly specialized subcircuits. Here, we used viral tracing, optogenetic-assisted patch clamping, chemogenetics and behavior in mice to examine changes in domain-defined hippocampus efferent projections from postnatal day (P)10 to P60. We found distinct anatomical and synaptic developmental signatures in ventral and intermediate CA1 downstream connectivity, with unique contributions to the prelimbic and infralimbic subregions of the medial prefrontal cortex (mPFC). Inhibition of the ventral CA1 (vCA1)-mPFC pathway during juvenility led to a deficit in adult cognitive flexibility exclusively in females, establishing a sex- and pathway-specific sensitive period preceding the stabilization of vCA1-mPFC synaptic transmission. Our data elucidate domain- and target-defined postnatal maturation of hippocampus efferents, identifying a sex-specific sensitive period with crucial implications for early life influences on adult cognition.

Keywords: Ventral CA1, intermediate CA1, electrophysiology, mice, cognitive flexibility, set shifting, optogenetics, chemogenetics.

Acknowledgements: This work was supported by a Natural Science and Engineering Council of Canada (NSERC) CGS-D (CGSD3 - 534884 – 2019) for AC-S, a grant from the NIH (R01MH126105) to CA, as well as grants from the Natural Science and Engineering Council of Canada (RGPIN-2017-06344), SickKids Foundation and Canadian Institutes of Health Research (CIHR) – Institute of Human Development, Child and Youth Health (NI19-1132R), CIHR (PJT 399790), and Human Frontier

Science Program Organization (CDA00009/2018 and RGY0072/2019) to MA-C. We acknowledge resources and support from the Centre for the Neurobiology of Stress (CNS) Core Facility at the University of Toronto Scarborough, and thank Durga Acharya and Bruno Chue for their help in the facility. A Canada Foundation for Innovation grant (#493864) was used to establish the Centre for the Neurobiology of Stress (CNS) Core Facility.

Author contributions: AC-S, AA, HC, RG and UM performed research. AC-S, AA, HC and MA-C analyzed data. MH and CA contributed to study design, data interpretation and writing of the paper. AC-S and MA-C designed research and wrote the paper.

Declaration of interests: The authors declare no competing interests.

Supplemental information:
Document S1: Figures S1–S7, Supplemental Table S1

Introduction

The hippocampus (HPC) plays a key role in learning and memory[1,2], anxiety-like behavior[3–5] and stress[6], with substantial evidence of distinct downstream pathway-specific contributions to these behaviors. Hippocampal projections to the lateral septum (LS) and basolateral amygdala (BLA) underlie fear memory processing and motivated behavior[7–9], while projections to the thalamic nucleus reuniens (Re) and medial prefrontal cortex (mPFC) are involved in working spatial memory and episodic memory[10–12]. Hippocampal projections to the nucleus accumbens (NAc) and lateral hypothalamus (LH) have been linked to anxiety, social interaction and feeding behavior[9,13]. HPC topographical organization across the septotemporal axis[14–16]

distinguishes three HPC domains: dorsal, intermediate and ventral HPC, which diverge in their cellular composition[17–21], efferent/afferent projection patterns[6,22,23], population encoding[24,25] and behavioral output[14,26–30]. This HPC tripartite differentiation is present from birth at both the gene expression and topographical afferent pattern levels[31,32], but very little is known about how the postnatal maturation of the HPC and its downstream projections diverge across its domains.

Early life is also the time of peak onset for neurodevelopmental and psychiatric disorders[51–53], which often feature deficits in the HPC and mPFC[54–61] and HPC-mPFC connectivity[62–66] in patients and animal models[49,56,68–70,57,58,62–67]. The HPC-mPFC pathway comprises unidirectional projections from the HPC intermediate and ventral domains to the mPFC[71–75], and supports decision making, reward learning, fear, and anxiety-like behaviors[11,36,76–78], all of which are (i) developmentally regulated[18,38] and (ii) implicated in neurodevelopmental and psychiatric disorders[36,79–81]. Furthermore, similar to the sensory cortex[82–85], both HPC[86–88] and mPFC[48–50,89–91] display heightened synaptic plasticity and behavioral features in early life consistent with critical periods, which may inform sensitivity to external influences such as stress[83,92–96,91]. Despite this convergence of factors in early life, it is unclear exactly how HPC-mPFC maturation may affect adult behavior and/or risk of neurodevelopmental and mental disorders.

Cognitive flexibility, or the ability to adjust behavior in response to changing conditions[97], is an essential facet of adaptive behaviour necessary for survival. Studies in humans broadly implicate the prefrontal cortex in cognitive flexibility[97–99], particularly in the case of extra-dimensional (ED) set shifting[100–102], a finding replicated in primates[103,104] and rodents[105–108]. Importantly, HPC lesions also feature deficits in ED

99 set shifting in humans[102]. In rodents, developmental manipulations of ventral HPC
100 impair ED set shifting[109,110] and alter mPFC morphology[110], implicating the HPC-mPFC
101 pathway in ED set shifting. While this is consistent with other research tying HPC-PFC
102 alterations to cognitive flexibility deficits in schizophrenia[111,112], the precise contribution
103 of HPC-mPFC pathways to higher-order cognitive flexibility remains unclear.

104 Despite important contributions to our understanding of HPC-mPFC oscillatory activity
105 in neonatal to juvenile mice[64,72,113,114], nothing is known about the postnatal
106 development of HPC-mPFC synaptic connectivity, or how this developmental trajectory
107 may affect adult cognitive function. To address this gap, we first compared the
108 developmental profile of intermediate and ventral CA1 innervation to brain regions
109 implicated in learning and memory (LS, BLA, mPFC, Re), social, anxiety- and
110 depression-like behavior (BNST, LH, NAc). We then resolved the synaptic maturation of
111 projections from ventral and intermediate CA1 to either prelimbic or infralimbic layer 5
112 mPFC pyramidal neurons using optogenetics-assisted patch clamping at postnatal day
113 (P)10, P15, P21, P30 and P60. Finally, we examined the functional implications of these
114 developmental changes by chronically inhibiting the vCA1-mPFC pathway during either
115 juvenility (P15-P30) or adulthood (P60-P75) and testing animals a month later in a
116 cognitive flexibility task. We found that inhibition of the vCA1-mPFC pathway led to a
117 sex-specific deficit in ED set shifting which was not present when the same inhibition
118 took place in adulthood. Together, these data establish a precise timeline for the
119 maturation of the HPC-mPFC pathway, highlighting septotemporal differences and
120 target-defined asynchronies in anatomical and synaptic maturation guiding sensitivity to
121 circuit disruption.

122 **Results**

123 ***Dorsal, intermediate and ventral CA1 neurons differ in their projection patterns in***
124 ***adult animals***

125 To understand the developmental timeline of HPC efferent pathway innervation, we first
126 compared the axonal terminal patterns of CA1 neurons from the dorsal, intermediate
127 and ventral HPC domains in adult mice. For consistency with subsequent analyses, we
128 infused the dCA1, iCA1 and vCA1 of P53 C57BL/6J mice with AAV1-ChR2-EYFP virus
129 and processed the brains one week later for histology (Fig. 1A), an interval previously
130 established by our group as sufficient for terminal transport[115]. Target regions were
131 chosen based on their involvement in the regulation of memory and emotional behavior:
132 NAc[116–118], LH[4], LS[119], BNST[120], BLA[4,121], Re[122] and mPFC[123–125]. Consistent with
133 previous reports[14,15,23,126–129], we saw domain-specific differences in CA1 efferent
134 innervation, particularly between dorsal and intermediate/ventral CA1 projections (Fig.
135 1). We found strong projections from iCA1 and vCA1 to mPFC (Fig. 1B), NAc core and
136 shell (Fig. 1C), LS (Fig. 1D), BLA (Fig. 1E), LH (Fig. 1F) and Re (Fig. 1G) which were
137 absent in dCA1-infused brains. We noticed strong projections from vCA1 to the BNST
138 (Fig. 1H), which were far weaker for iCA1 and absent for dCA1, as described in the
139 literature[130]. While all HPC domains send projections to the LS (Fig. 1D), the pattern of
140 LS innervations differs between dorsal and intermediate/ventral projections, with the
141 former predominantly innervating dorsomedial LS, and the latter the ventromedial LS
142 (Fig. 1D), as previously reported[131]. When we examined the mPFC, we saw strong
143 projections from both iCA1 and vCA1 spanning the prelimbic (PL) and infralimbic (IL)
144 subregions, with the strongest signal in IL layers 2/3 and 5, and PL layer 5 (Fig. 1B).

145 dCA1 axons in both PL and IL were only visible upon GFP signal amplification using
146 immunofluorescence (Fig. 1B, left). Accordingly, we were unable to evoke terminal
147 signals from this pathway when patching from either PL or IL pyramidal neurons,
148 suggesting the sparsity of dCA1-PFC projections may favour the outcome of some
149 experimental manipulations[132] over others.
150

151 ***Anatomical maturation of vCA1 and iCA1 projections across the lifespan***

152 Given the lack of overlap in the terminal projection patterns from dCA1 compared to
153 iCA1 and vCA1, we focused our efforts on comparing the maturation of iCA1 and vCA1
154 projections from infancy to adulthood. As ventral and intermediate CA1 projections
155 overlap across most targets tested, we wanted to assess whether these subprojections
156 would show equivalent maturation profiles, at both the anatomical and synaptic levels.
157 First, we quantified CA1 targeting across ages to ensure robust viral transduction
158 across ages and subprojections. Mice were injected with AAV1-ChR2-EYFP virus in
159 either vCA1 or iCA1 and brains were processed for histology one week later at P10,
160 P15, P21, P30 and P60 (Fig. 2A), corresponding to infancy, juvenility, late juvenility,
161 adolescence and adulthood, respectively[133]. We observed that in mice younger than
162 P15, vCA1 is very limited in total area compared to later ages, which precluded robust
163 targeting of vCA1 (but not iCA1) at P10 without spread to CA3 and neighboring areas.
164 Quantification of vCA1 infection area from P15 to P60 showed that the proportion of
165 infected vCA1 area (i.e. ratio of vCA1 EYFP volume and total vCA1 volume) was
166 equivalent across ages (Fig. 2B-C). The volume of infected vCA1 at P15 was lower than
167 all older ages (Fig. 2D, green; one-way ANOVA $p=0.0067$; post hoc $p<0.031$) to

168 compensate for hippocampal growth during this period (Fig. 2D, grey; one-way ANOVA,
169 p=0.0001; post hoc p< 0.013). There were no differences in vCA1 EYFP intensity (Fig.
170 2E) or sex differences in vCA1 volume across ages (Table S1).

171 Quantification of iCA1 infection showed a higher percentage of iCA1 targeted at P10,
172 but not among other age groups (Fig. 2F-G; one-way ANOVA p=0.0001; post hoc
173 p<0.036). This is likely driven by the significantly smaller volume of iCA1 at P10 (Fig.
174 2H, grey; one-way ANOVA p<0.0001; post hoc p<0.0022), despite a smaller iCA1
175 infected area at P10 compared to older ages (Fig. 2H, green; one-way ANOVA p=0.016;
176 post hoc p<0.047). We found no age-dependent differences in EYFP iCA1 intensity
177 (Fig. 2I) or sex differences in iCA1 volume across ages (Table S1).
178

179 *vCA1 and iCA1 terminals reach target regions by P10*

180 We next examined the age in which CA1 projections arrive to their target regions. vCA1
181 and iCA1 terminals were already present in all target regions by the earliest age tested
182 of P10 (Fig. S1). To determine at what precise age CA1 axon terminals arrive at the
183 mPFC, we infused RetroBeads into the mPFC and examined their transport to CA1 in
184 infant and adult mice (Fig. S2A). We first confirmed that a 5-day incubation period was
185 sufficient for retrograde transport from mPFC to CA1 in adult (8 weeks of age) mice
186 (Fig. S2B). CA1 soma signal was present exclusively at the posterior/temporal HPC, at
187 both the vCA1 and iCA1, but not at the anterior/septal (dorsal) HPC (Fig. S2B). We
188 found soma signal in the CA1 of P10 brains following this same injection interval (Fig.
189 S2C), consistent with our anterograde data (Fig. S1). We then tested the presence of
190 CA1-mPFC projections at the earlier age of P5. There was no soma signal at the HPC

191 of P5 brains (Fig. S2D), suggesting that CA1 axons arrive at the mPFC between P5 and
192 P10 in C57BL/6J mice.
193
194 *Distinct target-defined maturation signatures in vCA1 and iCA1 terminal density*

195 To characterize CA1 terminal density changes across ages, we quantified CA1 axon
196 terminal fluorescent intensity in the NAc, LS, BLA, LH, Re, BNST and mPFC (PL and
197 IL). vCA1 terminal density changed across ages within LS nuclei (Fig. 3A-C), showing a
198 peak at P21 in the LSD, LSV and LSI (Fig. 3A; LSD: one-way ANOVA $p=0.0005$; post
199 hoc test $p<0.015$; Fig. 3B; LSV: one-way ANOVA $p=0.0013$; post hoc $p<0.0040$; Fig.
200 3C; LSI: one-way ANOVA $p=0.0088$; post hoc $p = 0.0050$). vCA1 terminal density
201 showed a similar peak at P21 in the NAc core and shell (Fig. 3D; NAc core: one-way
202 ANOVA $p=0.036$; post hoc $p<0.05$; Fig. 3E; NAc shell: one-way ANOVA $p=0.012$; post
203 hoc $p<0.041$) and BNST (Fig. 3H; one-way ANOVA $p=0.021$; post hoc $p<0.039$), but
204 remained stable across ages in the BLA (Fig. 3F) and the Re (Fig. 3G). In contrast,
205 vCA1 terminal density in the LH was higher at P15 compared to P30 (Fig. 3I; one-way
206 ANOVA $p=0.024$; post hoc $p=0.017$). We saw no sex differences in any of the regions
207 examined (Table S1). These data suggest target-defined developmental changes in
208 vCA1 efferent anatomical connectivity, with vCA1 terminal density in regions such as
209 BLA and Re remaining stable from P15, while terminals in LSD, LSV, LSI, NAc, BNST
210 and LH undergo further refinement across ages, emphasized by a peak in vCA1
211 terminal density at P21 in most of these regions.

212 We next conducted a similar analysis targeting the iCA1 (Fig. 3J-Q). iCA1 terminal
213 intensity in the LSD and LSI decreased with age, starting at P21 in the LSD (Fig. 3J:

214 one-way ANOVA p=0.0092; post hoc p< 0.049), and between P10 and P60 in the LSI
215 (Fig. 3K: one-way ANOVA p=0.0153; post hoc p=0.0081). There were no iCA1
216 terminals in the LSV, indicating that vCA1 is the only source of LSV innervation across
217 the CA1 septotemporal axis. Counter to our results in the vCA1, iCA1 terminal intensity
218 remained stable across ages in the NAc core and shell (Fig. 3L-M), BLA (Fig. 3N), Re
219 (Fig. 3O) and BNST (Fig. 3P). Surprisingly, iCA1 terminal intensity in the LH was
220 greater at P60 compared to P10 (Fig. 3Q; one-way ANOVA p=0.0088; post hoc
221 p=0.019). We found sex differences in the Re (two-way ANOVA p=0.039; post hoc
222 p=0.012) and the LH (two-way ANOVA p=0.015; post hoc p = 0.0032), whereby males
223 displayed increased iCA1 terminal density compared to females at P21 (Table S1).
224 These data emphasize a contrast between a mostly stable pattern of iCA1 terminal
225 density across ages (with the exception of the LS and LH), and vCA1 terminal changes,
226 which displayed distinct timing (centered around P21, or juvenility), and more
227 widespread targets, also spanning the NAc and BNST. A graphical summary of these
228 findings is available in Fig. S3. Together, these data highlight sex- and domain-specific
229 time signatures of anatomical connectivity among HPC efferents.

230 We next quantified ventral and intermediate CA1 terminal density in the mPFC, focusing
231 on PL and IL layers 2/3, 5 and 6 (Fig. 4A, H). We saw no differences in vCA1 terminal
232 density from P15 to P60 in PL layers 2/3 (Fig. 4B), 5 (Fig. 4C) or 6 (Fig. 4D). We also
233 saw no age-dependent differences in vCA1 innervation of IL (Fig. 4E-G), or sex
234 differences (Table S1). Thus, in contrast to the refinements seen in other vCA1 target
235 regions, anatomical connectivity between vCA1 and PL/IL is stable from P15 onwards.

236 When we extended this analysis to iCA1 terminals (Fig. H-N), we found significant age-
237 dependent increases in iCA1 terminals in all PL layers starting at P30 (Fig. 4I-K; Layer
238 2/3: one-way ANOVA p=0.0006; post hoc p<0.0031; layer 5: one-way ANOVA
239 p=0.0009; post hoc p<0.020; layer 6: one-way ANOVA p=0.0085; post hoc p=0.0070).
240 These changes were not seen in IL (Fig. 4L-N). Interestingly, P21 males showed
241 increased terminal density in PL layer 5 compared to females (two-way ANOVA
242 p=0.013; post hoc p=0.0024; Table S1). These data suggest asynchrony in the
243 anatomical maturation of iCA1 terminals within the mPFC, with a delay in the
244 stabilization of iCA1 innervation of PL relative to IL, starting at adolescence.
245 Furthermore, these divergent maturation trajectories point to significant septotemporal
246 specialization in the anatomical maturation of iCA1 and vCA1 projections to mPFC,
247 whereby only iCA1 projections to PL display age-dependent changes between infancy
248 and adulthood.
249
250 ***Maturation of CA1-PFC synaptic transmission***

251 Dysfunction in the communication between the intermediate/ventral HPC and the mPFC
252 is a prominent feature of cognitive deficits in rodent models of neurodevelopmental
253 disorders[65], and yet very little is known about the developmental trajectory of synaptic
254 connectivity within this pathway[64,72,113,134]. To address this gap, we set out to investigate
255 the domain-specific synaptic maturation of CA1-mPFC pathways in C57BL/6J mice.
256
257 *Maturation of spontaneous transmission in PL and IL layer 5 pyramidal neurons*

258 To understand the context in which CA1 axons arrive and influence synaptic
259 transmission in the mPFC, we first investigated the maturation of spontaneous
260 excitatory and inhibitory synaptic transmission in layer 5 PL and IL pyramidal neurons at
261 P10, P15, P21, P30 and P60. Starting with the PL, we saw an increase in the amplitude
262 of spontaneous excitatory postsynaptic currents (sEPSCs) between P10-P21 to P30-
263 P60 (Fig. 5A-B; one-way ANOVA $p< 0.0001$; post hoc $p<0.032$), but no change in
264 sEPSC frequency (Fig. 5C) or tau decay time (Fig. 5D). When examining PL
265 spontaneous inhibition, we found a similar increase in the amplitude of spontaneous
266 inhibitory postsynaptic currents (sIPSCs) between P10-21 and P30-P60 (Fig. 5E: one-
267 way ANOVA $p<0.0001$; post hoc $p<0.045$) and an earlier increase in sIPSC frequency
268 starting at P21 (Fig. 5F; one-way ANOVA $p <0.0001$; post hoc $p<0.012$), but no change
269 in sIPSC decay time (Fig. 5G). A within-cell comparison of sEPSC and sIPSC PL
270 frequencies showed a shift toward increased relative sIPSC frequency at P30 and P60
271 (Fig. 5H; paired t-test $p<0.033$), which is replicated in the increase in the spontaneous I-
272 E frequency difference at P30 and P60 (Fig. 5I; one-way ANOVA $p=0.0042$; post hoc
273 $p<0.0480$). We saw sex differences in PL sEPSC and sIPSC amplitude (higher in P30
274 females and P60 males), tau decay time (higher in P30 males and P60 females), sIPSC
275 frequency (higher in males at P30 and P60), as well as spontaneous I-E frequency
276 differences, with P21 males and P60 females showing greater differences (Table S1).
277 These data point to significant pre- and postsynaptic changes in spontaneous inhibitory
278 transmission in PL layer 5 pyramidal neurons between P15-21 and P30, including a shift
279 toward increased spontaneous inhibition that is likely reflective of maturation of local
280 interneurons[135].

281 Parallel analysis of the maturation of IL layer 5 spontaneous transmission showed no
282 change in sEPSC amplitude (Fig. 5J-K) or tau decay time (Fig. 5M), but a peak in
283 sEPSC frequency at P21 compared to P10 and P60 (Fig. 5L; one-way ANOVA
284 p=0.0021; post hoc p<0.0073). IL layer 5 pyramidal neurons showed an increase in
285 sIPSC amplitude between P15 and P30 (Fig. 5N; one-way ANOVA p=0.049; post hoc
286 p=0.023), and an increase in sIPSC frequency from P21 (Fig. 5O; one-way ANOVA
287 p<0.0001; post hoc p<0.026) accompanied by a change in sIPSC tau decay time (Fig.
288 5P; one-way ANOVA p=0.019). Similar to PL, we saw an increase in the relative
289 frequency of spontaneous inhibition at P30-P60 (Fig. 5Q; paired t-test p<0.013) and
290 increased spontaneous inhibition to excitation differences between P10-15 and P60
291 (Fig. 5R; one-way ANOVA p=0.0023; post hoc p<0.0097), but no sex differences in this
292 dataset (Table S1). These data indicate synchronous changes in spontaneous inhibition
293 between PL and IL layer 5 neurons, with distinct maturation timelines for spontaneous
294 excitation between subregions.
295
296 *Asynchrony in the maturation of vCA1-PL and vCA1-IL presynaptic transmission*

297 To examine the maturation of pathway-specific CA1-mPFC synaptic transmission, we
298 injected AAV1-ChR2 virus into the ventral CA1 one week prior to recording from layer 5
299 pyramidal neurons in the PL or IL at P15, P21, P30 and P60 (Fig. 6A). To assess age-
300 dependent changes in glutamate release in these synapses, we analyzed EPSCs
301 during paired pulse stimulation, whereby the relative amplitude of the second response
302 is modulated by initial release probability. There was a significant decrease in paired
303 pulse ratios (PPR) of vCA1-PL synapses between P21 and later ages (Fig. 6B; Mixed-

304 effects model: main effect of age p=0.0009, interval x age interaction p<0.0001; post
305 hoc 100ms: p<0.029; 250ms: p<0.028; Fig. 6C; 250ms: one-way ANOVA p=0.0004;
306 post hoc p<0.0035), an effect largely driven by changes in females (two-way ANOVA
307 p=0.036; post hoc p=0.0024). This suggests an increase in vCA1-PL release probability
308 starting at adolescence. In contrast, vCA1-IL paired pulse ratios were equivalent across
309 all ages (Fig. 6D-E; no sex differences, Table S1), pointing to distinct presynaptic
310 maturation trajectories for vCA1 projections to these mPFC subregions, with the vCA1-
311 PL pathway showing a unique profile of presynaptic changes between P21 and P30 in
312 females.
313
314 *Projection-specific timing signatures for vCA1- and iCA1-mPFC presynaptic maturation*

315 Using an identical experimental setup, we next infused the iCA1 of mice with AAV1-
316 ChR2 virus and conducted patch clamp recordings one week later at P10, P15, P21,
317 P30 or P60 (Fig. 6J). There was a significant peak in iCA1-PL paired pulse ratios at
318 P15 compared to P10, P30 and P60 (Fig. 6K; Mixed-effects model: main effect of age
319 p=0.0003; post hoc 100ms: p<0.013; 250ms: p<0.021; 500ms: p<0.041; 1000ms:
320 p=0.048; Fig. 6L; 250ms: one-way ANOVA p= 0.0007; post hoc p< 0.011), suggesting a
321 relative increase in presynaptic efficacy in iCA1-PL synapses from P30. When we
322 examined iCA1-IL synapses, we saw a similar decrease in paired pulse ratio between
323 P15-P21 and P60 (Fig. 6M; Mixed-effects model: main effect of age p=0.0001; interval x
324 age interaction p=0.013; post hoc 100ms: p<0.024; 250ms: p<0.049; 500ms: p<0.041;
325 1000ms: p<0.020; Fig. 6N; 250ms: One-way ANOVA p=0.0022; post hoc p< 0.013).
326 These data suggest a slight delay in the refinement of presynaptic release probability in

327 iCA1-IL synapses (at P60) relative to vCA1-IL synapses (P15). There were no sex
328 differences in iCA1-IL paired pulse ratios (Table S1). Together, these results reveal a
329 differential time course for the presynaptic maturation of iCA1 and vCA1 projections to
330 mPFC subregions, with earlier maturation of iCA1-PL presynaptic efficacy (P21)
331 compared to vCA1-PL (P30). While vCA1-IL presynaptic changes reach adult levels by
332 P15 (earlier than iCA1-PL synapses), iCA1-IL synapses are relatively delayed, with a
333 significant change in paired pulse ratios only occurring at P60 (see Fig. S4, left panel for
334 a graphic summary of these data).
335
336 *Delayed maturation of iCA1-mPFC postsynaptic efficacy*

337 To examine changes in CA1 evoked *post*synaptic transmission in the mPFC, we next
338 recorded AMPAR currents and AMPA:NMDA ratios as a function of developmental age
339 in vCA1- and iCA1-PL and IL synapses using the same experimental design described
340 previously (Fig. 6A, J). We saw no change in the amplitude of AMPAR currents (Fig. 6F)
341 or in AMPA:NMDA ratios (Fig. 6G) in vCA1-PL synapses across ages. In vCA1-IL
342 synapses, there was a significant decrease in AMPAR response amplitude between
343 P15 and P60 (Fig. 6H; one-way ANOVA p=0.034; post hoc p=0.023) but no change in
344 AMPA:NMDA ratios (Fig. 6I; no sex differences, Table S1). While vCA1-mPFC
345 postsynaptic transmission remains largely stable between P10 and P60, iCA1-mPFC
346 postsynaptic maturation undergoes marked refinement across this period. There was no
347 change in the amplitude of AMPAR currents (Fig. 6O), but an increase in AMPA:NMDA
348 ratios between P15 and P30 (Fig. 6P; one-way ANOVA p= 0.019; post hoc p=0.020),
349 similar to the timeline of presynaptic changes. Analysis of iCA1-IL synapses showed a

350 decrease in AMPAR current amplitude (Fig. 6Q; one-way ANOVA p=0.0014; post hoc
351 p<0.025) and an increase in AMPA:NMDA ratios between P15 and P30-60 (Fig. 6R;
352 one-way ANOVA p=0.0048; post hoc p<0.020), indicating synchronous maturation of
353 postsynaptic efficacy (AMPA:NMDA ratios) of iCA1 synapses onto PL and IL
354 subregions, which occurs after the stabilization of vCA1-mPFC postsynaptic
355 transmission (from P15). Females showed larger vCA1-IL AMPAR current amplitude
356 compared to males at P15 (Table S1). Overall, these data show domain-, target-, and
357 synaptic locus-defined time signatures of synaptic maturation within the CA1-mPFC
358 pathway. While the vCA1-IL pathway remains stable across postnatal development,
359 vCA1-PL synapses display a dissociation between the timing of pre- and postsynaptic
360 refinement (increased PPR from P30 but stable AMPA:NMDA ratios across ages).
361 Within iCA1 projections, iCA1-IL synapses show a delayed onset of presynaptic
362 changes (P60) compared to postsynaptic changes (P30), but iCA1-PL synapses show
363 synchronous changes in PPR and AMPA:NMDA ratios. A visual summary of the evoked
364 CA1-mPFC synaptic maturation data is featured in Figure S4.
365

366 ***Inhibition of the vCA1-mPFC pathway during juvenility impairs adult cognitive***
367 ***flexibility***

368 We next wanted to probe the functional implications of the CA1-mPFC maturation
369 signatures identified by our anatomical and synaptic analyses. Critical periods in the
370 sensory cortex are marked by structural and synaptic changes[82,84,136–140], suggesting
371 that the timing of CA1-mPFC synaptic changes may signal similar sensitive periods in
372 its dependent behavior. To test this, we used an intersectional viral approach to

373 chemogenetically inhibit the vCA1-mPFC pathway at select developmental timepoints
374 and assess its effects on a cognitive flexibility behavioral task in adulthood (Figure 7A).
375 We injected a retrograde AAV virus expressing Cre recombinase into the mPFC and a
376 Cre-dependent inhibitory hM4Di AAV virus into the vCA1 to selectively inhibit the vCA1-
377 mPFC pathway via treatment with the agonist C21, which selectively activates hM4Di
378 receptors[141,142] (Figure 7A). As our electrophysiological data showed marked changes in
379 vCA1-PL presynaptic transmission between P21 and P30 in females, we targeted our
380 chronic inhibition to the juvenile period (P15-P30) in male and female mice, and
381 compared it to an identical manipulation during adulthood (P60-P75) (Figure 7A). After
382 30d, we tested the animals in an attentional set shifting task[106] for cognitive flexibility in
383 the absence of C21 (Figure 7A). In this task, mice learn to dig through two types of
384 bedding for a food reward. During rule acquisition, the food reward is associated with a
385 scent, regardless of bedding type (Figure 7A). After reaching criterion, animals undergo
386 an extradimensional set shifting test, in which the reward predictor switches to bedding
387 type (Figure 7A).

388 Mice that underwent vCA1-mPFC inhibition (hM4Di mice) during juvenility (P15-P30)
389 showed similar rates of rule acquisition of the set shifting task performed compared to
390 control mCherry mice in adulthood (Figure 7B). However, hM4Di females showed an
391 impairment in extradimensional set shifting (Figure 7C; two-way ANOVA effect of virus
392 and sex $p<0.0001$, interaction $p=0.0022$; post hoc $p<0.0001$). Importantly, juvenile-
393 inhibited female and male hM4Di-injected animals did not differ from mCherry-injected
394 mice in terms of time to first choice (Figure 7D) or distance travelled (Figure 7E) during
395 ED set shifting, suggesting that the ED set shifting deficit seen in the hM4Di females is

396 not driven by changes in exploration or motivation during the task. In the adult inhibition
397 cohort, which took place between P60-P75, male and female mCherry and hM4Di mice
398 showed similar performance at rule acquisition (Figure 7F) and in ED set shifting (Figure
399 7G-I), indicating that the ED set shifting impairment is specific to vCA1-mPFC pathway
400 disruption during juvenility. Importantly, chronic vCA1-mPFC inhibition in either cohort
401 did not affect performance or exploration in the elevated plus maze (Figure S5),
402 indicating that changes in anxiety-like behavior are not driving the ED set shifting deficit.
403 These findings identify a sex-specific sensitive period within the HPC-mPFC pathway
404 during early life that is crucial for cognitive flexibility in adulthood.
405

406 **Discussion**

407 Here we used a combination of viral tracing, optogenetic-assisted patch clamping,
408 chemogenetics and behavior to examine septotemporal differences in HPC afferent
409 projections across the lifespan, and their implications for cognitive function in adulthood.
410 This is to our knowledge the first demonstration of a pathway-specific sensitive period
411 for cognitive function. We found that the timing of anatomical refinement of CA1 axons
412 varied both according to the target region and within the CA1 septotemporal axis. While
413 CA1 projections to IL, BLA and Re remained stable from P10 to P60, vCA1 and iCA1
414 terminal density displayed distinct timing signatures in the PL, LS, NAc, BNST and LH.
415 Focusing on the synaptic maturation of CA1-mPFC projections, we saw an earlier onset
416 of changes in presynaptic transmission in iCA1-PL compared to vCA1-PL synapses,
417 with the opposite occurring between vCA1- and iCA1-IL synapses. Developmental
418 changes in postsynaptic transmission also showed asynchrony among these pathways,

419 with a marked delay within iCA1-PL and -IL synapses compared to vCA1 inputs. Finally,
420 we uncovered a sex-specific sensitive period for the vCA1-mPFC pathway during
421 juvenility, leading to cognitive flexibility deficits in adulthood. Overall, our data
422 consolidate a blueprint for the maturation of CA1-mPFC projections with crucial
423 implications for behavior and the effects of circuit disturbances and/or other factors
424 influencing circuit output from early life.

425 Our anatomical analysis showed unique timing of developmental signatures in vCA1
426 and iCA1 terminal density in the LS, NAc, BNST, LH and mPFC. While iCA1 terminal
427 density in LSD and LSI was the highest at P10, vCA1 terminal density across LS
428 subregions peaked at P21. In rats, HPC projections shift from medial septum to LS at
429 embryonic and perinatal (P1 and P5) stages[8,143], but less is known about HPC-LS
430 maturation following that period. Interestingly, in contrast to our vCA1 data, subiculum
431 projections to the LS increase in density between P0-P30 in the rat[144], suggesting
432 possible species and/or subregion developmental differences. We also saw a peak in
433 vCA1 innervation of NAc core and shell and BNST around P21, indicating coordinated
434 changes across most vCA1 targeted areas that undergo postnatal refinement within this
435 timeframe (but note the LH as an exception). In contrast, postnatal iCA1 terminal
436 density displays different afferent and temporal patterns. While iCA1 terminal pruning
437 occurs synchronously across LS subregions from P10 to later ages, projections to PL
438 increase in density with age, similar to the LH. In rats, the first 2 to 3 postnatal weeks
439 mark major changes in PL cytoarchitecture and an increase in dendritic
440 arborization[37,145,146], which may be informed by changes in afferent innervation including
441 from iCA1. While local expression of DCC/netrin guides pathway-specific anatomical

innervation trajectories within mesocortical pathways[147–150], the precise signaling molecules guiding the timing and region-specific differences in CA1 anatomical maturation still need to be identified. Importantly, the consistency of collateral patterns seen among certain adult vCA1 subpopulations[151] may contribute to the synchrony between vCA1 terminal changes reported here. Accordingly, Kim and Cho found that 9% of vCA1 neurons project to both mPFC and BLA[127], regions that showed similar maturation patterns in our analysis.

Our data on age-dependent changes in spontaneous EPSCs and IPSCs at PL layer 5 showed a significant shift towards increased global presynaptic inhibition at P30. Our findings are largely consistent with work by Kroon and colleagues which described an increase in sEPSC and sIPSC frequencies between P13-16 and P26-30 in PL layer 5[146], with similar increases also noted elsewhere[146]. However, Kroon and colleagues report relatively increased excitatory responses compared to ours[146], with differences in the age of the animals or in mouse strain/vendor possibly contributing to this disparity. Our data showed a significant shift toward PL and IL spontaneous inhibitory activity by P21-30, which is consistent with the timing of maturation of inhibitory interneurons in the mPFC between juvenility and adolescence[152–154]. Given the important role of mPFC inhibitory transmission in juvenility and adolescence to adult function[155], dissecting the relative contributions of select input pathways to mPFC interneurons in early life will be key to elucidating the factors regulating this potential sensitive period.

We established that iCA1 and vCA1 axons arrive at the mPFC between P5 and P10 in C57BL/6J mice. This is in line with neonatal studies that report HPC oscillatory influence on the mPFC as early as P7 in rats[72,156,157]. Although the physiology of glutamatergic

465 monosynaptic projections from the vCA1 to mPFC is well-known in adult mice[127,158–160],
466 very little was known about synaptic transmission within the CA1-mPFC circuit in early
467 life. Following the initial arrival of CA1 axons, we saw marked pathway- and age-
468 dependent changes in CA1-mPFC evoked synaptic activity. Specifically, the major
469 changes occurring in CA1-PL transmission within the second and third postnatal weeks
470 coincide with a P7-P13 shift from presynaptic depression to facilitation in PL layer 5
471 pyramidal cells following layer 2/3 stimulation in rats[161], as well as the maturation of
472 mPFC fast spiking interneurons and their increase in connectivity with pyramidal
473 neurons in the second postnatal week[154]. Importantly, this period also comprises major
474 changes in mPFC network oscillatory activity[154,156] and strengthening of HPC-mPFC
475 coupling between P8-10 and P16-24[64]. Moreover, changes in CA1 synaptic composition
476 across this same timeline[162] emphasize the need to understand the contribution of
477 developmental changes in synapse structure to the maturation of synaptic connectivity
478 as reported here.

479 Our previous work had shown a distinct temporal profile for the anatomical and synaptic
480 maturation of the mPFC-BLA pathway, which display a delayed arrival and refinement
481 of axons compared to CA1-mPFC projections, but synchronous evoked synaptic
482 changes around P30[115]. Interestingly, iCA1-PL, iCA1-IL and mPFC-BLA pathways
483 display an identical timeline of postnatal maturation of AMPA:NMDA ratios, suggesting
484 that pre- and postsynaptic maturation programs might be differentially expressed across
485 specialized projections. Altogether, these analyses point to a high degree of
486 specialization in the developmental profiles across brain pathways, whose guiding
487 principles remain unknown. Given the developmental milestones taking place from

488 juvenility to adolescence, including increased exploration and threat exposure upon
489 leaving the nest[163], understanding how these time signatures relate to specialized
490 stimulus processing and behavioral output needs further investigation.

491 We found that the timing of changes in vCA1-mPFC synaptic transmission marked a
492 sensitive period in the effects of pathway disruption on cognitive flexibility. This effect
493 was exclusive to females, in line with sex-specific changes in vCA1-PL PPR ratio
494 between juvenility and adolescent. While the origin and extent of this sex-specific effect
495 in vCA1-mPFC maturation trajectory and sensitivity remains unclear, these data add to
496 a growing literature showing sex differences in various aspects of HPC and mPFC
497 maturation[164–168], and in early life vulnerability to morphological, electrophysiological
498 and synaptic plasticity changes in both the HPC[169–171] and mPFC[95,172–175]. Interestingly,
499 the sex differences in our dataset were restricted to PL maturation of spontaneous
500 excitation and inhibition, as well as changes in vCA1-PL and iCA1-PL PPR, pointing to
501 mPFC subregion selectivity. Furthermore, pubertal onset of psychiatric disorders has
502 been linked to changes in cognitive flexibility[176–179], as well as changes in mPFC (and
503 CA1[180]) perineuronal nets[181] and increased inhibition[178] in females, factors known to
504 modulate sensitive periods[182–184]. Given the earlier onset of puberty in female mice
505 relative to males[178,185], which spans our intervention window, this may bear an important
506 influence over our results.

507 Previous studies had implicated mPFC function in the same ED set shifting task of
508 cognitive flexibility, with a key role for mPFC parvalbumin interneuron activity from P14-
509 P50 in adult ED set shifting performance[155]. While this timing overlaps with that of our
510 manipulation, the contribution of local mPFC interneurons to our findings is unknown.

511 Furthermore, inhibition of mediodorsal thalamus (MD) from P20-P50 leads to similar ED
512 set shifting impairments, which were accompanied by a reduction in mPFC sEPSC
513 frequency and in the density of thalamus-mPFC projections in adulthood[106], suggesting
514 that both vCA1- and MD-mPFC pathways exert a developmental influence on adult
515 cognitive flexibility. Intriguingly, layer 2/3 PL pyramidal neurons receive convergent input
516 from both MD and vHPC, while input to interneurons is biased: parvalbumin
517 interneurons receive relatively more input from MD and VIP interneurons from the
518 vHPC[186]. The exact interplay of these pathways and their modulation of developmental
519 sensitivity to disruption should be further explored. Additionally, a recent study showed
520 that systemic disruption of microglia activity from P28-P37 in mice led to changes in
521 mPFC network function and deficits in attentional set shifting rule acquisition and
522 reversal learning in adulthood[187]. While ED set shifting was not assessed, this suggests
523 the timing of this sensitive period might extend onto adolescence, while raising the
524 question of whether HPC input to mPFC is sensitive to microglial manipulation.
525 Importantly, this developmental timeline is also consistent with that reported for the
526 effects of amphetamine (P22-P31) on adult mPFC dopaminergic innervation and
527 behavioral inhibition[150,188], further establishing this period as one of broad sensitivity to
528 mPFC-related circuit function and behavior.

529 While these studies, together with ours, support a sensitive period from juvenility to
530 adolescence for mPFC-dependent cognitive function in adulthood, neonatal mPFC
531 disruptions have also been linked to behavioral deficits. Transient optogenetic activation
532 of mPFC from P7-11 leads to social, recognition and working memory deficits in
533 juvenility and adolescence, which are accompanied by changes in mPFC morphology,

534 electrophysiology and oscillations[189]. Additionally, serotonin transporter blockade from
535 P2-P11 disrupts mPFC morphology, neuronal excitability and anxiety- and depression-
536 like behavior[90]. Interestingly, the same group recently implicated serotonergic input to
537 the mPFC in ED set shifting[190], urging future research to explore the degree of overlap
538 (if any) between serotonergic and vCA1 terminals onto mPFC pyramidal neurons.

539 As research continues to refine knowledge of the topography and function of HPC
540 projections[127,151], the sex- and pathway-specific interrogation of the postnatal
541 development of HPC pathways adds a crucial layer to improving our understanding of
542 brain-behavior relationships and their contribution to the physiology of emotional and
543 cognitive function across the lifespan.

544

545 **Figures and Figure Legends:**

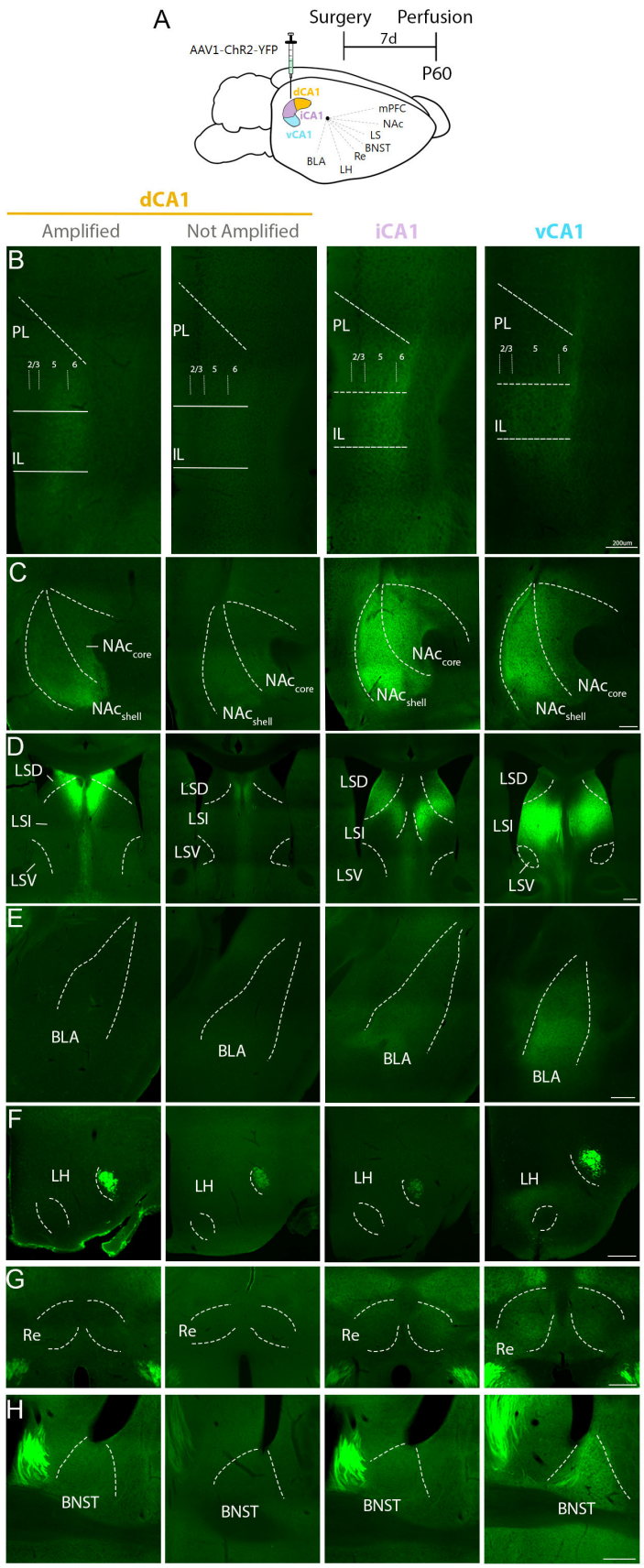
A
Surgery
Perfusion
7d
P60
AAV1-ChR2-YFP
dCA1
iCA1
vCA1
mPFC
NAc
LS
BNST
Re
BLA
LH
dCA1
Amplified
Not Amplified
iCA1
vCA1
B
PL
2/3
5
6
IL
C
NAc core
NAc shell
D
LSD
LSI
LSV
E
BLA
F
LH
G
Re
H
BNST

546

547 **Figure 1. Comparison of projection patterns from dorsal, intermediate and ventral**
548 **CA1. A**. C57BL/6J mice were injected with AAV-ChR2-YFP virus in the dorsal,
549 intermediate or ventral CA1 and perfused seven days later at P60 for tissue and image
550 processing. **B-H.** Qualitative differences between projections from dCA1 (left image
551 columns) and those from intermediate iCA1 (middle image column) and vCA1 (right
552 most column), with the iCA1 and vCA1 projections showing largely similar patterns
553 across examined regions. The left most column of images (dCA1 amplified) underwent
554 immunohistochemistry against GFP to amplify viral signal. All other images show direct
555 fluorescence under identical settings. BNST = bed nucleus of the stria terminalis, BLA =
556 basolateral amygdala, IL = infralimbic cortex, LH = lateral hypothalamus, LSD = dorsal
557 lateral septum, LSI = intermediate lateral septum, LSV = ventral lateral septum; NAc =
558 nucleus accumbens, PL= prelimbic cortex, Re = thalamic nucleus reuniens. Scale bar:
559 200μm.

560

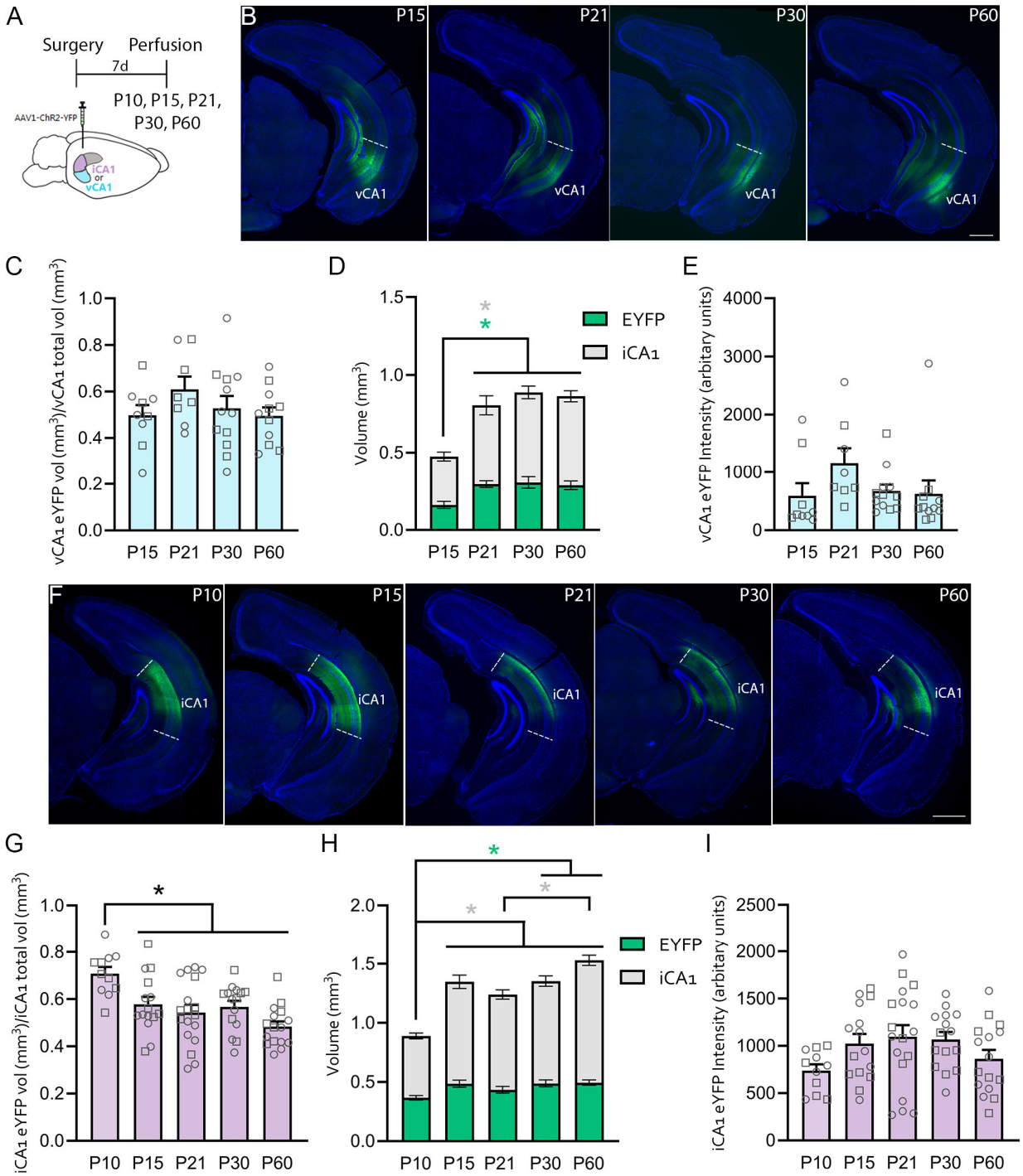

Figure 2. Targeting vCA1 and iCA1 across ages. A. C57BL/6J mice were injected with AAV-ChR2-YFP virus in either the vCA1 (**B-E**) or iCA1 (**F-I**) and perfused seven days later at P10, P15, P21, P30 or P60 for tissue and image processing. **B**. Sample images of AAV1-ChR2-EYFP infusion at the vCA1 in P15, P21, P30 and P60 mice. **C**. Estimated proportion of total vCA1 volume (mm^3) with EYFP infection for each age group. **D**. Estimated total vCA1 volume (grey) and EYFP infected vCA1 volume (green) for all age groups. **E**. Average intensity of infected EYFP vCA1 area for each age group.

F. Sample images of AAV1-ChR2-EYFP infusion at the iCA1 in P10, P15, P21, P30 and P60 mice. **G**. Estimated proportion of total iCA1 volume (mm^3) with EYFP infection for each age group. **H**. Estimated total iCA1 volume (grey) and EYFP infected iCA1 volume (green) for all age groups. **I**. Average intensity of infected EYFP iCA1 area for each age group. Individual female datapoints are represented as circles, and males as squares. Scale bars: 500μm. * p <0.05. Grey and green asterisks in **D** and **H** represent statistical significance in the total region volume and EYFP volume datasets, respectively. For full n values and break-down of all figures, refer to Table S1.

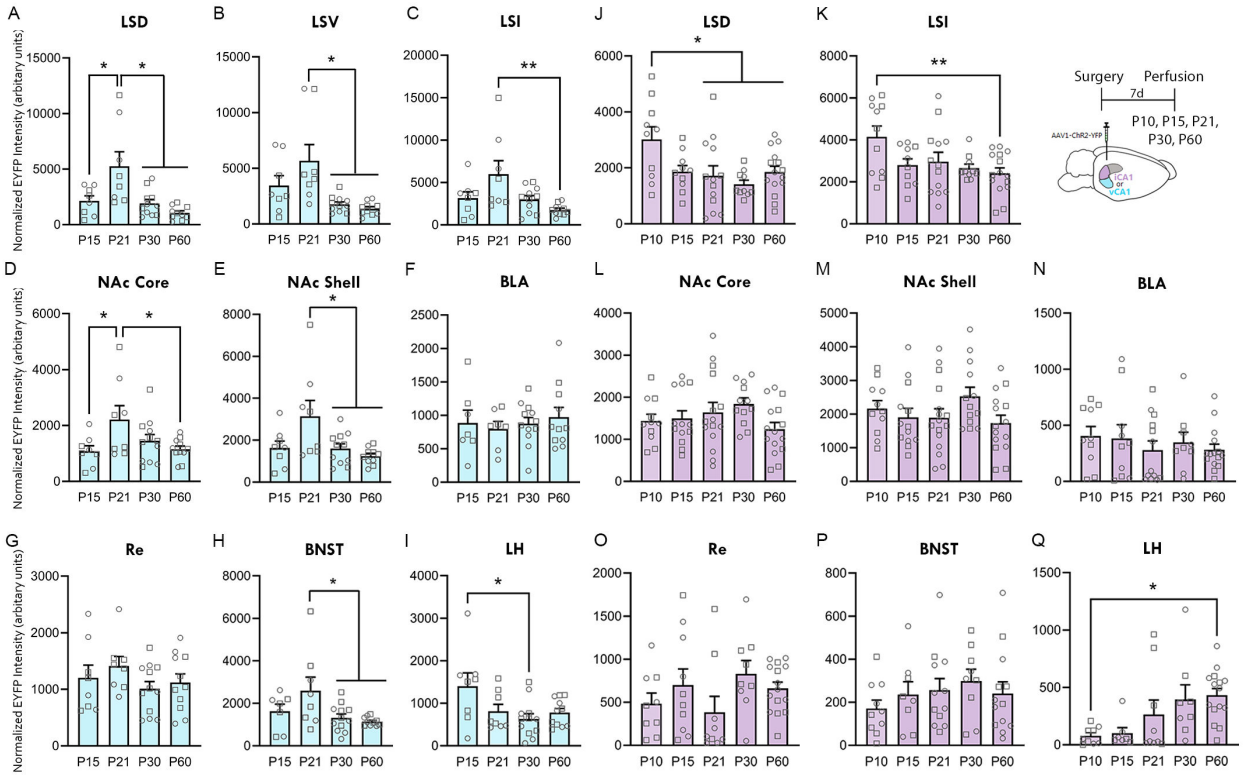

Figure 3. Pathway-specific developmental changes in vCA1 and iCA1 terminal density. C57BL/6J mice were injected with AAV-ChR2-YFP virus in the vCA1 (**A-I**) or the iCA1 (**J-Q**) and perfused seven days later at P10, P15, P21, P30 or P60 for tissue and image processing. **A-I**. Normalized average vCA1 terminal intensity across ages at the dorsal lateral septum (LSD; **A**), ventral lateral septum (LSV; **B**), intermediate lateral septum (LSI; **C**), nucleus accumbens (NAc) core (**D**) and shell (**E**); basolateral amygdala (BLA; **F**), thalamic nucleus reuniens (Re; **G**), bed nucleus of the stria terminalis (BNST; **H**), and lateral hypothalamus (LH; **I**). **J-Q**. Normalized average iCA1 terminal intensity across ages at the LSD (**J**), LSI (**K**), NAc core (**L**) and shell (**M**), BLA (**N**), Re (**O**), BNST (**P**), and LH (**Q**). Individual female datapoints are represented as circles, and males as squares. *p<0.05. **p<0.01.

591

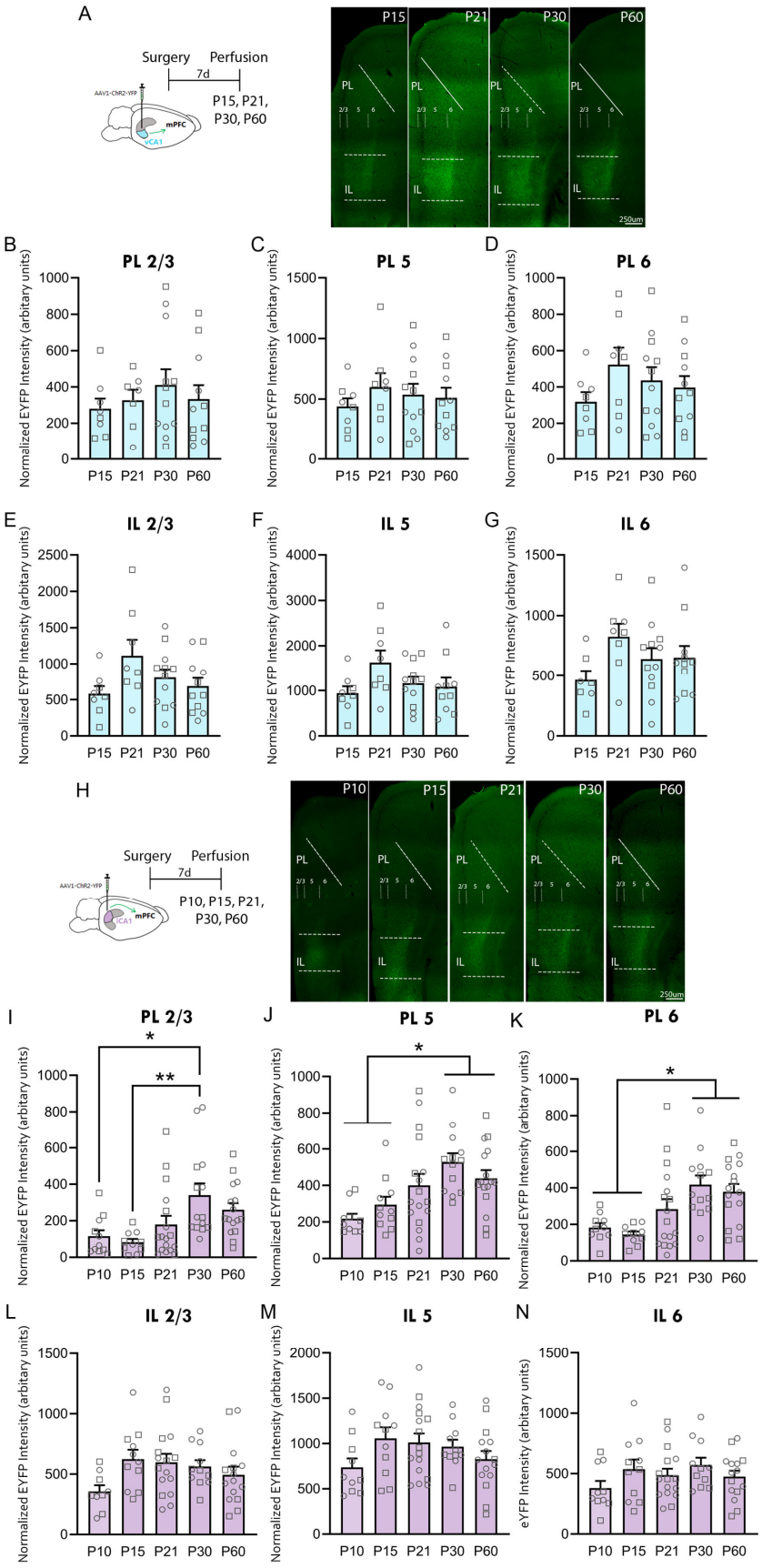
A
Surgery
Perfusion
7d
P15, P21, P30, P60
AAV1-ChR2-YFP
mPFC
CA1
P15
P21
P30
P60
PL
IL
2/3
5
6
250um
B
PL 2/3
C
PL 5
D
PL 6
E
IL 2/3
F
IL 5
G
IL 6
Normalized EYFP Intensity (arbitary units)
P15
P21
P30
P60
H
Surgery
Perfusion
7d
P10, P15, P21, P30, P60
P10
I
PL 2/3
J
PL 5
K
PL 6
L
IL 2/3
M
IL 5
N
IL 6
eYFP Intensity (arbitary units)
P10
P15
P21
P30
P60

592

593 **Figure 4. vCA1 terminal density is stable in PL and IL across postnatal**
594 **development, but iCA1 terminal density increases in PL starting at adolescence.**
595 **A**. *Left*: Experimental design for the vCA1 experiments. C57BL/6J mice were injected
596 with AAV-ChR2-YFP virus in the vCA1 and perfused seven days later at P15, P21, P30
597 or P60 for tissue and image processing. *Right*: Sample images of vCA1 projections
598 present at the medial prefrontal cortex in P15, P21, P30 and P60 mice (numbers
599 indicate cortical layers). **B-D**. Quantification of vCA1 terminal intensity across ages in
600 PL layers 2/3 (**B**), 5 (**C**) and 6 (**D**)**. E-G**. Average vCA1 terminal intensity for all age
601 groups at IL layers 2/3 (**E**), 5 (**F**) and 6 (**G**). **H**. *Left:* Experimental design and sample
602 images for the iCA1 experiments. C57BL/6J mice were injected with AAV-ChR2-YFP
603 virus in the iCA1 and perfused seven days later at P10, P15, P21, P30 or P60 for tissue
604 and image processing. *Right*: Sample images of iCA1 projections present at the mPFC.
605 **I-K**. Age-dependent differences in iCA1 terminal intensity in PL layers 2/3 (**I**), 5 (**J**) and 6
606 (**K**)**. L-N**. Average iCA1 terminal intensity for all age groups at IL layers 2/3 (**L**), 5 (**M**)
607 and 6 (**N**). Individual female datapoints are represented as circles, and males as
608 squares. Scale bar: 250μm. *p<0.05, ** p<0.01. PL = prelimbic cortex. IL = infralimbic
609 cortex.

610

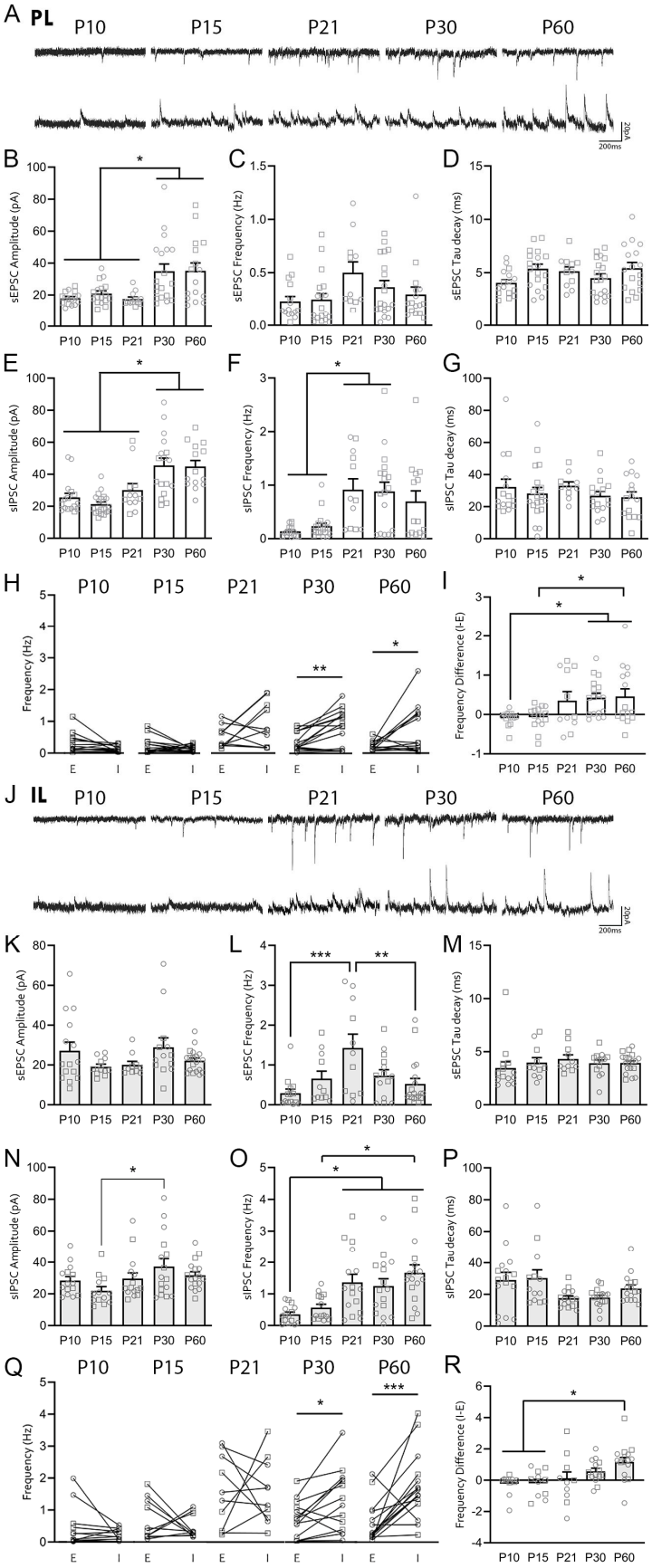
A PL
P10
P15
P21
P30
P60
20pA
200ms
B
sEPSC Amplitude (pA)
C
sEPSC Frequency (Hz)
D
sEPSC Tau decay (ms)
E
sIPSC Amplitude (pA)
F
sIPSC Frequency (Hz)
G
sIPSC Tau decay (ms)
H
Frequency (Hz)
E I
I
Frequency Difference (I-E)
J IL
K
L
M
N
O
P
Q
R

611

612 **Figure 5. Maturation of PL and IL layer 5 Pyramidal Cell Spontaneous Activity. A-I**.
613 Age-dependent changes in PL layer 5 pyramidal neuron spontaneous excitatory and
614 inhibitory postsynaptic currents (sEPSCs and sIPSCs) from P10 to P60. Example traces
615 **(A),** sEPSC amplitude (**B**), frequency (**C**) and tau decay (**D**). sIPSC amplitude (**E**),
616 frequency (**F**) and tau decay (**G**). **H**. Within-cell comparison of sEPSC and sIPSC
617 frequencies. **I**. Spontaneous I-E frequency difference (calculated by subtracting sEPSC
618 frequency from sIPSC frequency). **J-R**. Maturation of IL layer 5 Spontaneous Activity.
619 Example traces (**J**)**,** sEPSC amplitude (**K**), frequency (**L**) and tau decay (**M**). Maturation
620 of IL sIPSC amplitude (**N**), frequency (**O**) and tau decay (**P**). **Q**. Within-cell comparison
621 of relative sEPSC and sIPSC frequencies. **R.** Spontaneous I-E frequency difference.
622 Individual female datapoints are represented as circles, and males as squares. ***** p
623 <0.05 ** p<0.01 *** p<0.001.

624

625

626

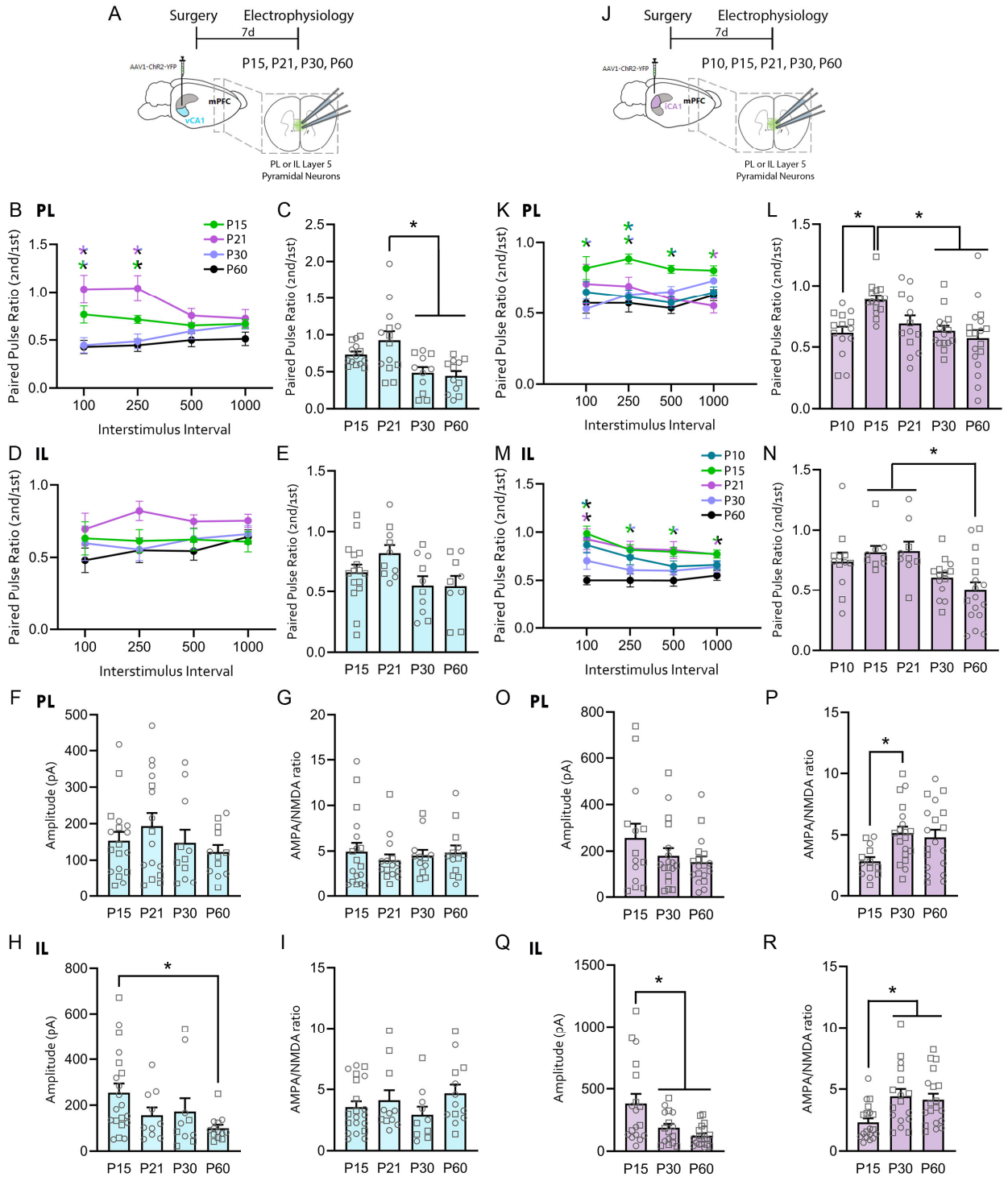

627

628 **Figure 6 Asynchronous pre- and postsynaptic strengthening of vCA1- and iCA1-**
629 **PL and IL synapses.** C57BL/6J mice were injected with AAV-ChR2-YFP virus in the
630 vCA1 (**A-I**) or the iCA1 (**J-R**) and seven days later at P15, P21, P30 or P60 underwent
631 patch clamp recordings from PL or IL layer 5 pyramidal neurons upon blue light LED
632 stimulation. **A**. Experimental design for vCA1 experiments. **B-E**. Comparison of paired
633 pulse ratio (second/first response) in PL layer 5 pyramidal neurons across intervals (**B**)

634 and at 250ms interstimulus interval (**C**). **D-E.** Paired pulse ratios from IL layer 5
635 pyramidal neurons across intervals (**D**) and with 250ms interval (**E**). **F-G**. vCA1-PL layer
636 5 AMPAR current amplitude (**F**) and AMPA:NMDA ratios (**G**) across ages. **H-I.** vCA1-IL
637 AMPAR amplitudes (**H**) and AMPA:NMDA ratio (**I**). **J**. Experimental design for iCA1
638 experiments. **K-L**. Paired pulse ratios in iCA1-PL synapses across interstimulus
639 intervals (**K**) and at 250ms interstimulus interval (**L**). **M-N.** Paired pulse ratios in iCA1-IL
640 synapses across intervals (**M**) and with 250ms interval (**N**). **O-R**. iCA1-PL AMPAR
641 current amplitude (**O**) and AMPA:NMDA ratios (**P**). **Q-R**. iCA1-IL AMPAR current
642 amplitude (**Q**) and AMPA:NMDA ratios (**R**). Individual female datapoints are
643 represented as circles, and males as squares. *p <0.05. * Represents a difference
644 between P21 and P30/P60; * between P15 and P60; * between P15 and P21/P30;
645 * between P15 and P10; * between P15 and P10/P60; * between P10/P15 and
646 P60; * between P15 and P30/P60; * between P15/P21 and P60; * between P21
647 and P60, and * between P15 and P21.

648

649

650

651

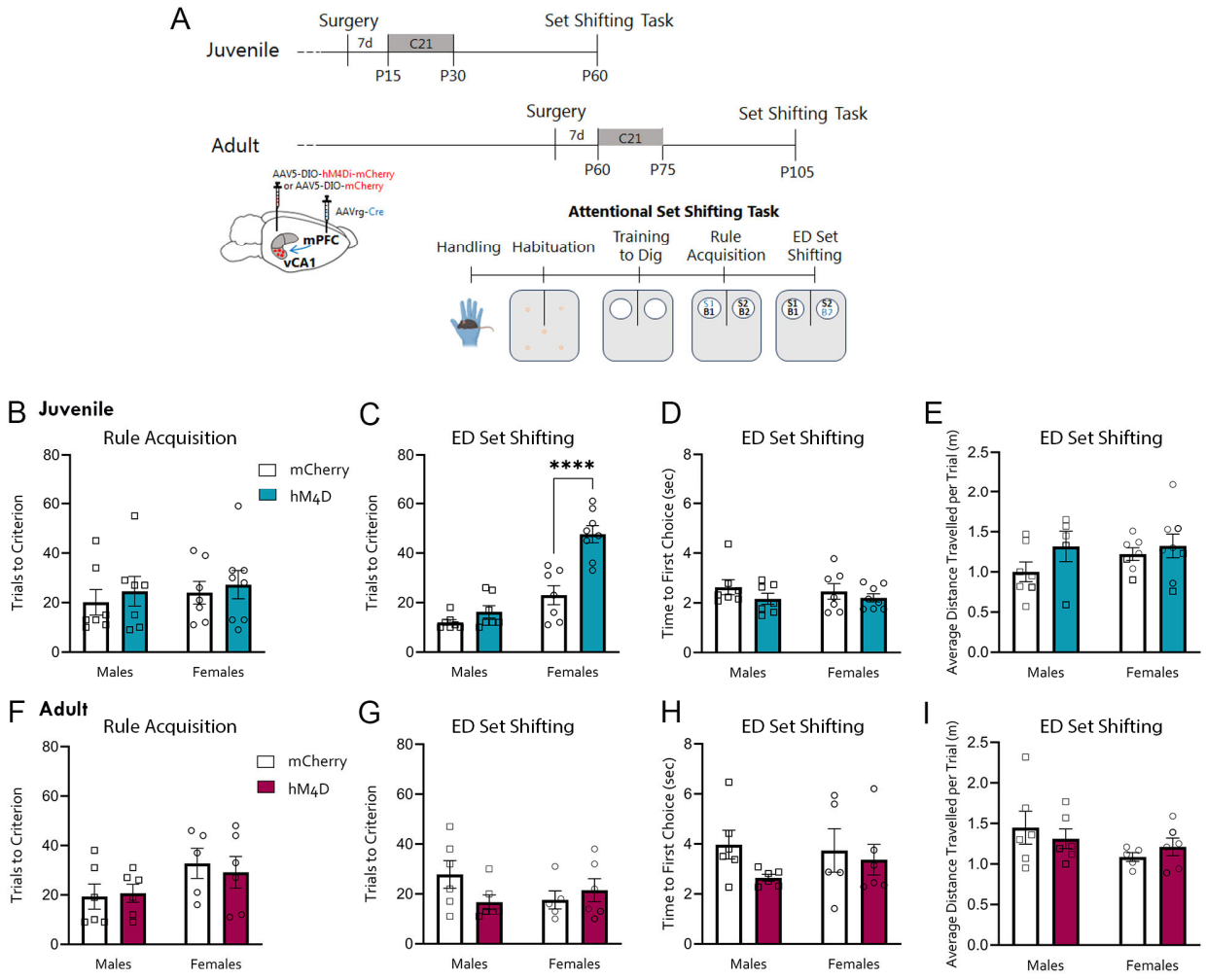

Figure 7. vCA1-mPFC inhibition during juvenility, but not adulthood, impairs extradimensional set shifting in females. A. Experimental design. Mice were injected with a retrograde AAV expressing Cre recombinase (AAVrg-Cre) in the mPFC and Cre-dependent hM4D or mCherry (AAV-DIO-hM4D-mCherry or AAV-DIO-mCherry) in the vCA1 7d prior to chronic treatment with the DREADD agonist C21 for 15d either during the *juvenile* period (from P15-P30) or in *adulthood* (separate cohort receiving equivalent C21 injections from P60-P75). 30d later, animals underwent attentional set shifting[105,106]. Following handling, habituation and training to dig sessions, animals learned an association (rule learning) between a scent and a food reward (rewarded contingency marked in blue). The next day, animals underwent an extradimensional (ED) set shifting test in which the reward was paired with the bedding type. All groups underwent set shifting in adulthood in the absence of C21. **B-E**. Juvenile cohort. Number of trials to criterion at rule learning (**B**) and ED set shifting (**C**). Time to first choice (**D**) and distance travelled (**E**) during ED set shifting. **F-I**. Adult cohort. Number of trials to criterion at rule learning (**F**) and ED set shifting (**G**). Time to first choice (**H**) and distance travelled (**I**) during ED set shifting. Individual female datapoints are represented as circles, and males as squares. ****p<0.0001.

670

671 **Methods**

672 Animals

673 C57BL/6J (Jackson Laboratory) mice were bred at the University of Toronto
674 Scarborough and kept on a 12h light/dark cycle (lights on at 07:00 h) in a standard static
675 cage on ¼" corncob bedding with access to food and water *ad libitum*. Date of birth was
676 designated postnatal day (P)0, with litter sizes ranging from 2 to 11 pups. At 21 days
677 (P21) mice were weaned and housed in same-sex littermate groups of 2 to 5 mice.
678 Littermates were randomly assigned to experimental groups, with each litter distributed
679 across ages tested counterbalanced for sex. All experiments were conducted during the
680 light cycle. Approximately equal numbers of females and males were used for all
681 experiments. All animal procedures were approved by the Animal Care Committee at
682 the University of Toronto.

683 Stereotaxic surgery and viral injections

684 C57Bl/6J mice underwent stereotaxic surgery at P3, P8, P14, P23 or P53. 0.12-0.25μL
685 of AAV1-CaMKIIa-hChR2(H134R)-EYFP virus was infused at the iCA1 bilaterally for
686 each age group (P3: AP-2.5, ML-/+2.65, DV-2.5; P8: AP-2.60, ML-/+3.15, DV-3.00;
687 P14: AP-2.65, ML-/+ 3.2, DV-3.00; P23: AP-2.7, ML-/+3.4, DV-3.00; P53: AP-2.75, ML-
688 /+3.6, DV-3.00). For vCA1 experiments, 0.12-0.2μL of AAV1-CaMKIIa-hChR2(H134R)-
689 EYFP virus was infused at the vCA1 bilaterally at P8, P14, P23 or P53 (P8: AP-2.46,
690 ML-/+3.05, DV-4.60; P14: AP-1.9, ML-/+ 3.1, DV-4.6; P23: AP-2.42, ML-/+3.1, DV-4.60;

691 P53: AP-2.53, ML-/+3.25, DV-4.5). For dCA1 experiments, 0.2uL of AAV1-CaMKIIa-
692 hChR2(H134R)-EYFP virus was infused at the dCA1 bilaterally at P53 (AP-2.1, ML-
693 /+1.50, DV-1.50). Hypothermia was used as an anesthetic for surgeries taken place at
694 P3. Mice older than P8 were injected intraperitoneally (i.p.) with a combination of
695 ketamine (100 mg/kg) and xylazine (5 mg/kg) to induce anesthesia. Once anesthetized,
696 the head was shaved and swabbed with iodine followed by 70% ethanol. Tear gel
697 (Alcon) was applied to the eyes to prevent dehydration. Mice were then secured in a
698 rodent stereotaxic apparatus (Stoelting) using ear bars. Body temperature was
699 maintained throughout surgery with a heating blanket. An incision was made down the
700 midline of the scalp using a scalpel, the connective tissue was excised, and then the
701 skull was cleaned with sterile phosphate buffered saline (PBS, pH=7.4). An autoclaved
702 cotton-tip applicator was briefly submerged in 30% hydrogen peroxide and gently
703 applied to the skull surface to identify bregma. After surgery, mice recovered for one
704 week and then were transcardially perfused or underwent slice electrophysiology
705 (details described below). For the retrograde tracing surgeries, mice at P0, P5 or aged
706 8-9 weeks underwent stereotaxic surgery (as above) infusing, bilaterally, red Lumafluor
707 RetroBeads™ at the mPFC (P0: AP+0.3, ML-/+0.2, DV-0.75; P5: AP+1.07, ML-/+0.25,
708 DV-2.6; Adult: AP+2.0, ML-/+0.3, DV-2.8). Five days after surgery, mice underwent
709 transcardial perfusion (details described below). For the set shifting experiments, mice
710 at P8 or P53 underwent stereotaxic surgery (as described above) infusing bilaterally,
711 pAAV5-hSyn-DIO-hM4D(Gi)-mCherry or pAAV5-hSyn-DIO-mCherry at the vCA1
712 (coordinates for P8 and P53 above) and pENN-AAV-hSyn-Cre-WPRE-hGH
713 (Retrograde) at the mPFC (P8: AP+1.52, ML-/+0.26, DV-2.5; P53: AP+2.0, ML-/+0.3,

714 DV-2.8). After surgery, mice recovered for one week prior to commencing chronic C21
715 injections (procedure described below).

716 Perfusions and sectioning

717 Mice were injected with Avertin (250mg/kg, i.p.) and once under deep anesthesia,
718 transcardially perfused with approximately 50mL of room temperature 0.1M PBS
719 (pH=7.4), followed by approximately 80mL of cold 4% paraformaldehyde (PFA). Brains
720 were extracted and stored overnight at 4°C in 4% PFA. Brains were subsequently
721 sectioned at 50µm in the coronal plane (VT1000, Leica) and stored at -20 °C in a
722 cryoprotectant solution comprised of 60% glycerol and 0.01% sodium azide in PBS.

723 Immunohistochemistry

724 Immunostaining was performed on free floating sections. Sections were washed in 0.1M
725 PBS (3 x 5 min each) and then incubated in blocking solution comprising 5% normal
726 goat serum and 0.25% Triton X-100 in 0.1M PBS for 30 min. For the amplified dCA1
727 brains, amplification of the viral signal was achieved by incubating sections with
728 polyclonal chicken anti-GFP (1:1000, #ab13970; Abcam, RRID: AB_300798) primary
729 antibody diluted in blocking solution. Sections were incubated overnight at 4 °C on a
730 rotary shaker under gentle agitation. On the following morning, sections were incubated
731 in goat anti-chicken Alexa 488 (1:1000, #A11039, Invitrogen, RRID: AB_2534096)
732 secondary antibody for 2 hours and Hoechst 33342 nuclear dye (1:1000 diluted in 0.1M
733 PBS; #H1399; ThermoFisher). Sections were then rinsed in 0.1M PBS, mounted onto
734 gelatin-coated slides and coverslipped with Permafluor anti-fade mounting medium
735 (#TA030FM; Thermo Scientific).

736 Anatomical maturation analysis

737 Brains were sectioned (50µm thickness) with a VT1000S vibratome (Leica). All sections
738 were stained with nuclear dye Hoechst 33342 (1:1000) for 10 min at room temperature.
739 Sections were mounted onto slides, air dried, and coverslipped with anti-fade mounting
740 medium (as described above) and imaged using a Nikon Eclipse Ni-U Upright
741 epifluorescent microscope. iCA1 and vCA1 projection-associated EYFP fluorescence
742 was quantified by measuring average pixel intensity for each in region of interest and
743 subtracting the background/basal measure of intensity. Internal baseline measures of
744 intensity for each section were taken from the motor cortex/frontal associative cortex
745 which are devoid of temporal hippocampal projections[128]. An average intensity
746 difference was calculated from both hemispheres using ImageJ/FIJI software (NIH, MD,
747 USA; https://imagej.net/software/fiji/). Regions of interest included: the prelimbic cortex
748 (PL) (layer 2/3, 5 and 6), infralimbic cortex (IL) (layer 2/3, 5 and 6), nucleus accumbens
749 (NAc) (shell and core), lateral septum (LS) (dorsal, ventral and intermediate nucleus),
750 basolateral amygdala (BLA), lateral hypothalamus (LH), thalamic nucleus reuniens (Re)
751 and the bed nucleus of the stria terminalis (BNST). Whole area intensity was measured
752 for each region. Comparisons were made of iCA1/vCA1 projection-associated EYFP
753 intensity at these regions among the different age groups. All calculated intensities were
754 normalized with total iCA1 or vCA1 volume.

755 To ensure viral spread is restricted only to, and covers the whole of the iCA1 or vCA1,
756 the Cavalieri method [($V_c = d(\Sigma(y_i))$, where V_c = estimated volume (mm^3), d = distance
757 between sections (µm) and y = area of EYFP infection or iCA1/vCA1 per section (mm^2)]
758 was used to estimate, for each age, viral spread and total iCA1/vCA1 volume. The iCA1

759 is defined as the dorsal CA1 ($dCA1^i$) region (pyramidal, oriens and radiatum layers) that
760 begins from bregma -2.70mm and terminates at -3.88mm labelled in Franklin & Paxinos
761 mouse atlas[191]. For sections that do not have the CA2 region that easily delineates the
762 $dCA1^i$ on the dorsal-ventral axis within bregma -2.70 to -3.88mm, the $dCA1^i$ consisted of
763 the CA1 area above the rhinal fissure/bottom limit of the perirhinal cortex[191]. This
764 boundary follows the lower border of the intermediate CA1 set by Dong et al. (2009) and
765 Fanselow & Dong (2010). Since these authors found that their iCA1 region and
766 temporal/posterior dCA1 region follow the same pattern of gene expression[192], for this
767 study, the iCA1 encompasses both Dong et al. (2009)'s posterior dCA1 and iCA1.
768 Estimated volume of EYFP and iCA1/vCA1 were compared between each age group to
769 corroborate the reduction of hippocampal mass and the restriction of viral spread at
770 earlier ages[115]. Results are expressed as percentage of estimated EYFP volume and
771 iCA1/vCA1 volume.

772 Slice electrophysiology

773 Mice were anesthetized with isoflurane and perfused transcardially with ice-cold (0°C–
774 4°C) sucrose solution composed of (in mM): 197 sucrose, 11 glucose, 2.5 KCl, 1.25
775 NaH2PO4, 25 NaHCO3, 0.4 ascorbate, 1 CaCl2, 4 MgCl2 and 2 Na pyruvate. Acute
776 350 μm coronal slices of PFC were obtained from dissected brains using a VT1000S
777 vibratome (Leica) and then incubated at 35°C for 25 min in the same solution, but with
778 50% standard artificial cerebral spinal fluid (ACSF) composed of (in mM): 120 NaCl, 2.5
779 KCl, 1.25 NaH2PO4, 25 NaHCO3, 11 glucose, 2 CaCl2, 1 MgCl2 and 2 Na pyruvate.
780 Following recovery, slices were maintained at room temperature in standard ACSF.
781 Whole-cell voltage-clamp recordings were obtained from principal pyramidal neurons in

782 layer 5 PL or IL using borosilicate glass electrodes (3–5 MΩ). Electrode internal solution
783 was composed of (in mM) of the following: 130 Cs-methanesulfonate, 10 HEPES, 0.5
784 EGTA, 8 NaCl, 4 Mg-ATP, 1 QX-314, 10 Na-phosphocreatine, and 0.4 Na-GTP.
785 Pyramidal excitatory neurons in the mPFC were discriminated on the basis of soma
786 size, high capacitance (>200 pF), and slow EPSC kinetics, under the rationale that no
787 interneuron subtypes possess all three of these characteristics. CA1 axon terminals
788 were stimulated using illumination with a digital multimirror device (Polygon400,
789 Mightex) and a TTL-pulsed microscope objective-coupled light-emitting diode (LED, 470
790 nm, 14 mW/mm2, Mightex). This pulse intensity evoked maximal response amplitudes
791 at all ages. For analysis of AMPA/NMDA ratios, we applied 1 μM TTX (#HB1035,
792 HelloBio) and 100 μM 4-AP (#AB120122, Abcam) for more stringent isolation of
793 monosynaptic transmission [115,193,194]. Paired pulse evoked EPSC and spontaneous
794 EPSCs and IPSCs were conducted in standard ACSF described above. Paired pulse
795 evoked EPSC were recorded using a low chloride internal (TEA-Cl 5mM). Data were
796 low-pass filtered at 3 kHz (evoked) and 10 kHz (spontaneous) and acquired at 10 kHz
797 using Multiclamp 700B and pClamp 10 (Molecular Devices). All stimulation was
798 conducted at 0.1 Hz to avoid inducing synaptic plasticity. Series and membrane
799 resistance was continuously monitored, and recordings were discarded when these
800 measurements changed by >20%. Recordings in which series resistance exceeded 25
801 MΩ were rejected. Detection and analysis of sEPSCs and sIPSCs were performed blind
802 to experimental group using MiniAnalysis (Synaptosoft). EPSC decay time constants (τ
803 decay) were obtained by standard exponential curve fitting of averaged current traces in

804 Clampfit (Molecular Devices). AMPA/NMDA ratio was calculated as the peak EPSC at -
805 70 mV divided by the EPSC amplitude at 100ms after current onset at +40 mV[115,193].

806 C21 injections

807 Animals were injected for 16 days consecutively with DREADD agonist compound 21
808 (C21; 2mg/kg, 0.5mg/mL, i.p.; #HB6124; HelloBio)[141], twice a day[106], once at 8:30 am ±
809 1 hour and once at 4:30 pm ± 1 hour, ensuring an 8-hour gap in between. The juvenile
810 group was injected from P15-P30, and the adult group was injected from P60-P75.
811 These cohorts underwent attentional set shifting in the absence of C21.

812 Behavioural testing

813 *Attentional Set Shifting Task*

814 *Apparatus:* A rectangular chamber made of white plexiglass (14.5 cm x 16.5 cm) was
815 separated by a 20 cm long x 16.5 cm wide x 0.5 cm thick plexiglass wall with two 19.2
816 cm wide x 17.8 cm long adjoining sliding doors on either lateral side to enclose the
817 mouse in the left or right upper quadrant. The apparatus was elevated 41 cm off the
818 floor with an Imaging Source DMK 22AUC03 1.1.3 IR camera mounted 88.4 cm directly
819 above it using a wall mount rack. An external LED lamp (280 Lux) was positioned
820 adjacent to the camera and 87.4 cm above the chamber to evenly distribute light. Two
821 round ceramic saucers each measuring 8.9 cm in diameter were placed in the chamber
822 at each of the quadrants during testing (at a 2.8 cm distance from each lateral wall and
823 7.6 cm away from the sliding door). The saucers were filled with one of two types of
824 bedding [counterbalanced; bark (Zoo Med Repti Bark) or cellulose paper (Biofresh 1/8"

825 Pelleted Cellulose) bedding], mixed with either a garlic or cinnamon powder
826 (McCormick), one of which predicted the reward location. Four different variations of
827 scent–bedding mixtures were used: bark–cinnamon, bark–garlic, paper–cinnamon and
828 paper–garlic.

829 *Procedure:* We used a variation of the protocol described by the Kellendonk group[105,106].
830 Animals were assessed in adulthood at P56-P61 for the juvenile group and at P101-
831 P106 for the adult group. Animals started undergoing food deprivation on the first day of
832 handling (Day 1). Mice were handled for 2 days (twice per day for 2 minutes, Days 1-2).
833 On Day 2, after the second habituation session, mice underwent one 10-minute
834 habituation session in which they were exposed to the experimental apparatus in the
835 presence of cheerios spread across the chamber to encourage exploration (no saucers
836 present). Starting on the day after habituation (Day 3), mice underwent two days of
837 training to dig (6 trials/day), when they learn to dig in the saucer filled with bed-o-cob
838 bedding for a cheerio reward. The bedding amount was increased incrementally over
839 the six daily sessions until the cheerio was fully covered. On the following day (Day 5),
840 animals underwent rule acquisition. During rule acquisition, animals were exposed to
841 two saucers displaying a pseudorandom, counterbalanced combination of one of the
842 two beddings and scents, one of which contained a cheerio reward. The reward was
843 paired with one of the scents (rule; counterbalanced) for the first five warm-up trials until
844 they found the cheerio. From trial six onwards, once the animal's snout crossed the
845 edge of the saucer, this was considered a decision, which was followed by enclosing
846 the animal within the side of the chamber for 30 seconds using a sliding door. Trials ran
847 until animals reached the criterion of 8 correct choices within 10 consecutive trials,

848 taken as a proxy for learning the scent–reward association. The next day (Day 6), mice
849 underwent extradimensional (ED) set shifting. During ED set shifting, a similar
850 procedure from rule acquisition was followed, but the bedding medium (instead of the
851 scent) predicted the cheerio location. Trials ran until animals reached the criterion of 8
852 correct choices within 10 consecutive trials. Animals that did not meet this criterion
853 before reaching 70 trials were excluded from the experiment. Scent and bedding types
854 were counterbalanced between animals. Trials were recorded using the Imaging Source
855 DMK 22AUC03 1.1.3 IR camera and distance travelled and time to first choice were
856 quantified using ANYmaze software (Stoelting, USA). Trials to criterion were quantified
857 manually by a blind experimenter and validated through ANYmaze. Two juvenile hM4D
858 animals showed an outlier profile for distance travelled during set shifting (3.78m and
859 3.98m), which was solely driven by exploration after choice (while eating the food
860 reward) and were therefore excluded from that analysis.

861

862 QUANTIFICATION AND STATISTICAL ANALYSIS

863 Data are presented as mean ± SEM with n shown as the number of animals for
864 histological experiments, or number of cells followed by number of animals in
865 parenthesis for electrophysiological experiments. Due to space limits, only significant p
866 is reported in the main text, with all other detailed statistical analyses (including sex
867 differences) reported in Table S1. All statistical analyses were performed in GraphPad
868 Prism® version 9 through one-way ANOVA or two-way repeated-measures ANOVA,
869 where appropriate. Omnibus test results (F values) are reported in Table S1. To test for

870 group differences following ANOVA, we applied the software default of Tukey's or
871 Bonferroni-corrected post hoc tests for all pairwise comparisons following non-repeated
872 and repeated measures ANOVA, respectively, and significant results were denoted by
873 asterisks in associated figures. Potential sex differences were first assessed using a
874 two-way, repeated measures ANOVA and in the absence of effects, data were
875 collapsed across these variables for subsequent analyses. Outliers were detected using
876 the software outlier test (Grubbs' Test or the extreme studentized deviant method) and
877 removed from the dataset prior to running group and/or post hoc comparisons.

878

879 KEY RESOURCES TABLE

REAGENT or RESOURCE	SOURCE	IDENTIFIER
Antibodies		
Monoclonal rat anti-mCherry (#M11217)	ThermoFisher	RRID: AB_2536611
Polyclonal rabbit anti-cFos (#226 003)	Synaptic Systems	RRID: AB_2231974
Goat anti-rat Alexa 568 (#A11077)	ThermoFisher	RRID: AB_2534121
Donkey anti-rabbit horseradish peroxidase (#711-036-152)	Jackson ImmunoResearch	RRID: AB_2340590
Polyclonal chicken anti-GFP (#AB13970)	Abcam	RRID: AB_300798
Goat anti-chicken Alexa 488 (#A11039)	Invitrogen	RRID: AB_2534096
Hoechst 33342 nuclear dye (#H1399)	ThermoFisher	
Bacterial and virus strains		
AAV1-CaMKIIa-hChR2(H134R)-EYFP	Addgene	# 26969-AAV1
Red RetroBeads	LumaFluor Inc	R170
pENN-AAV-hSyn-Cre-WPRE-hGH (Retrograde)	Addgene	#105553-AAVrg
pAAV5-hSyn-DIO-hM4D(Gi)-mCherry	Addgene	#44362-AAV5
pAAV5-hSyn-DIO-mCherry	Addgene	#50459-AAV5
Experimental models: Organism/strains		

Mouse: C57BL/6J	The Jackson Laboratory	
Chemicals, peptides, and recombinant proteins		
Ketamine (Narketan 100 mg/mL Vial/10 ml)	CDMV	#032N
Xylazine (AnaSed 100 mg/mL Btle/ 50ml)	CDMV	#113537
Avertin (2% 2,2,2-tribromoethanol + tert-amyl alcohol in 0.1M PBS)	Sigma-Aldrich	#T48402 #240486
Tetrodotoxin citrate, Na+ channel blocker, 1mg (TTX)	HelloBio	#HB1035
4-Aminopyridine, K+ channel blocker, 100mg (4-AP)	Abcam	#AB120122
Compund-21, water soluble (C21)	HelloBio	#HB6124
Software		
ImageJ/Fiji	NIH, MD, USA	https://imagej.net/software/fiji/
ANYmaze	Stoelting Company	#60605
MiniAnalysis (Synaptosoft)		

880

881

882

883

884

885

886

887

888

889

890 **Supplemental Figures and Legends:**

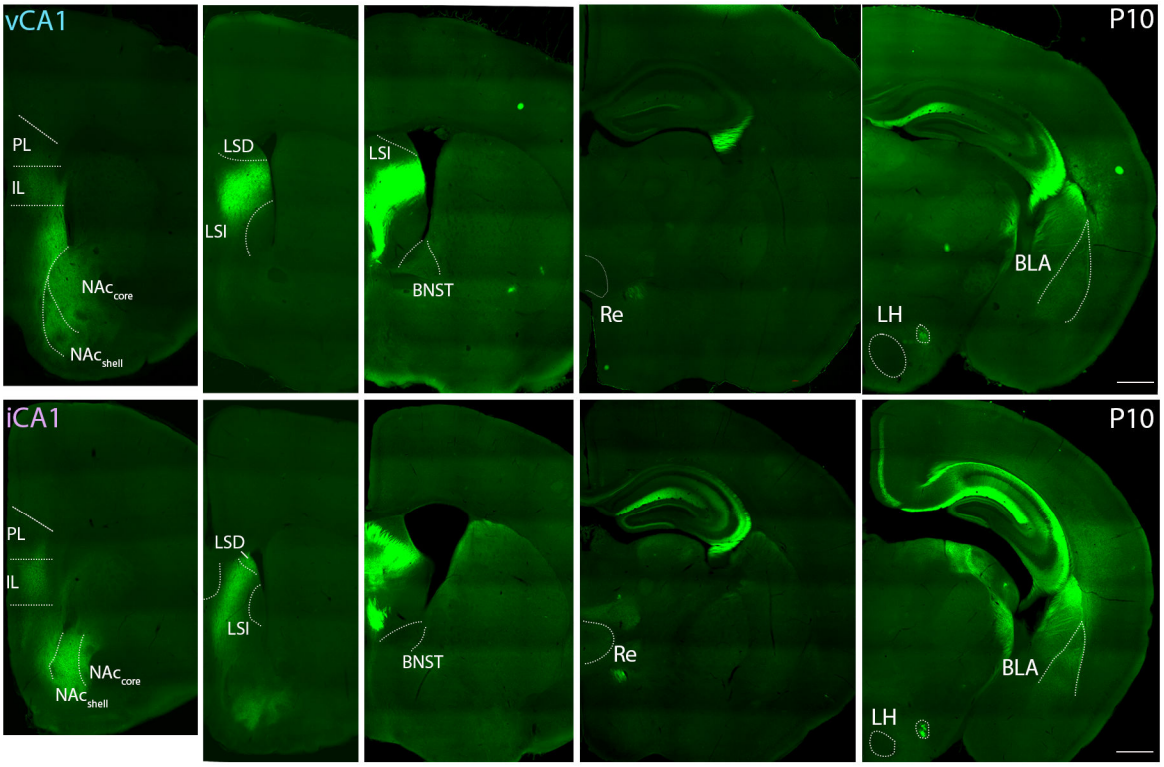

891

892 **Figure S1. iCA1 and vCA1 axons are already present in all target areas by P10.**
893 C57BL/6J mice were injected with AAV-ChR2-YFP virus in the ventral (vCA1) or
894 intermediate (iCA1) CA1 at P3 and perfused seven days later at P10 for tissue and
895 image processing. vCA1 (top panel) and iCA1 (bottom panel) axons were already
896 visible at P10 in the prelimbic cortex (PL), infralimbic cortex (IL), nucleus accumbens
897 (NAc) core and shell, dorsal lateral septum (LSD) and intermediate lateral septum (LSI),
898 thalamic nucleus reuniens (Re), basolateral amygdala (BLA), bed nucleus of the stria
899 terminalis (BNST), and lateral hypothalamus (LH). Scale bar: 500μm.

900

901

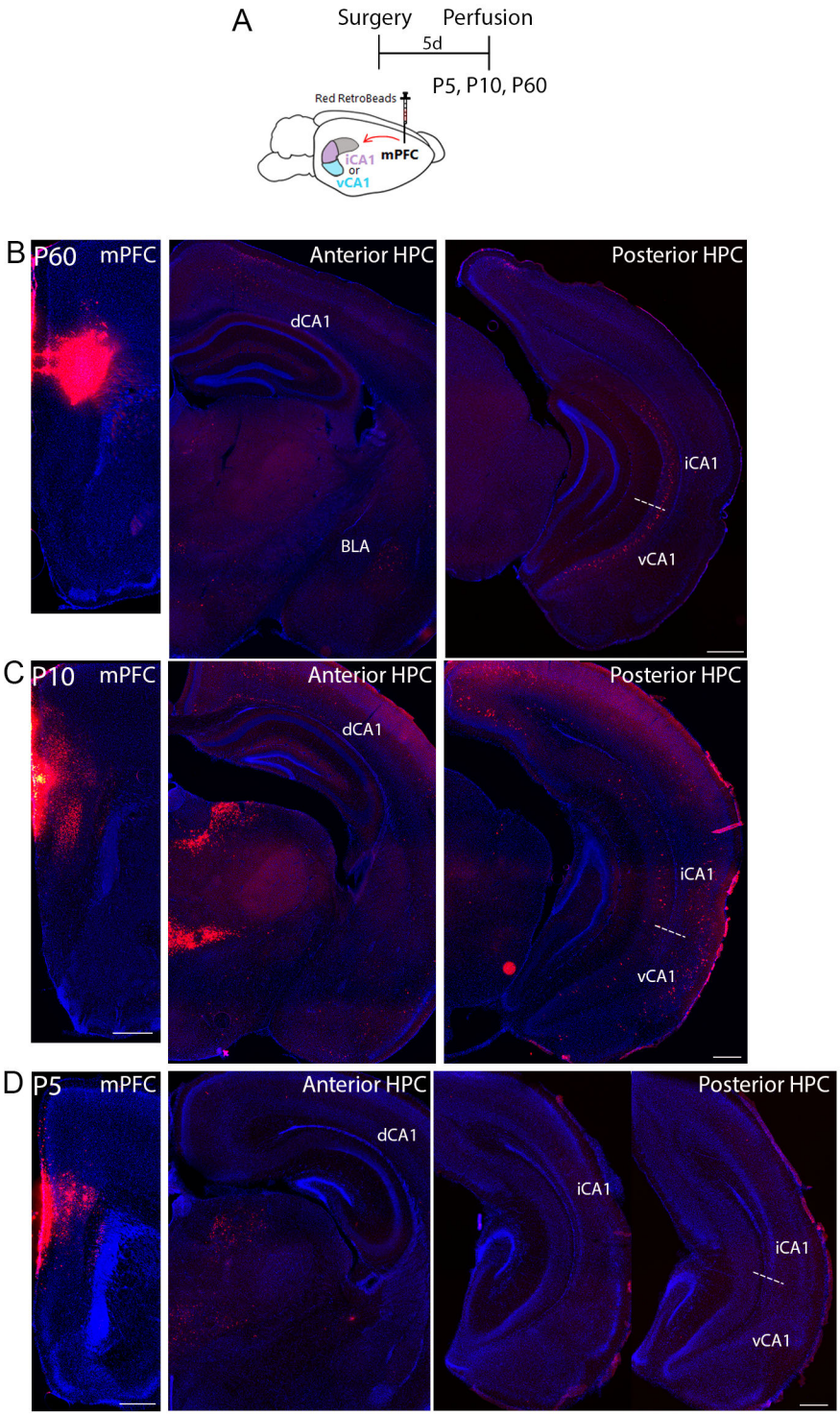

Figure S2. CA1 terminals arrive at the mPFC between P5 and P10 in C57BL/6J mice. A. Schematic of experiment. C57BL/6J mice were infused with red Lumafluor RetroBeads™ bilaterally at the medial prefrontal cortex (mPFC). Mice were transcardially perfused 5 days following surgery at P5, P10 or P60. **B**. Sample image of the mPFC infusion site in an adult P60 brain (*left most image*) shows absence of red

soma signal at the dorsal CA1 (dCA1) but labeled cells in the basolateral amygdala (BLA) (*center image*) and in the intermediate CA1 (iCA1) and ventral CA1 (vCA1) (*right most image*). **C**. Sample image of the mPFC infusion site in a P10 brain (*left most image*) showing absence of red soma signal at the dCA1 but labeled cells in the BLA (*center image*), as well as in the iCA1 and vCA1 (*right most image*). **D**. Sample image of the mPFC infusion site in a P5 brain (*left most image*) showing absence of red soma signal at the dCA1, iCA1 or vCA1 (*right most images*). Scale bar: 500μm.

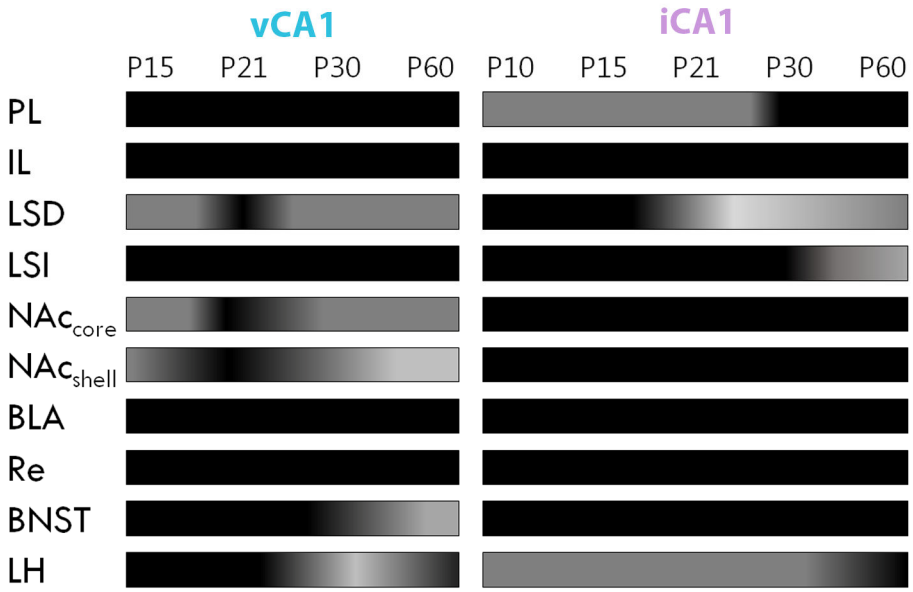

Figure S3. Graphic representation of anatomical maturation data for vCA1 and iCA1 projections. Rectangular heatmaps represent relative changes in terminal density across respective ages, whereby darker color represents an increase. PL = prelimbic cortex, IL = infralimbic cortex, NAc = nucleus accumbens, LSD = dorsal lateral septum, LSI = intermediate lateral septum, Re = thalamic nucleus reuniens, BLA = basolateral amygdala, BNST = bed nucleus of the stria terminalis, LH = lateral hypothalamus.

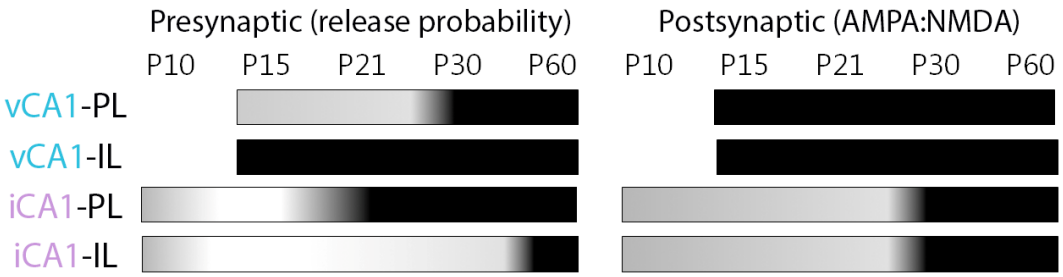

Figure S4. Graphic representation of evoked synaptic maturation data for vCA1- and iCA1- PL and IL pathways. Rectangular heatmaps represent relative changes in presynaptic (**Left**; or release probability, the inverted function of the paired pulse ratios) and postsynaptic efficacy (**Right**, represented as AMPA:NMDA ratios) across respective ages, whereby darker color represents an increase. PL = prelimbic cortex, IL = infralimbic cortex.

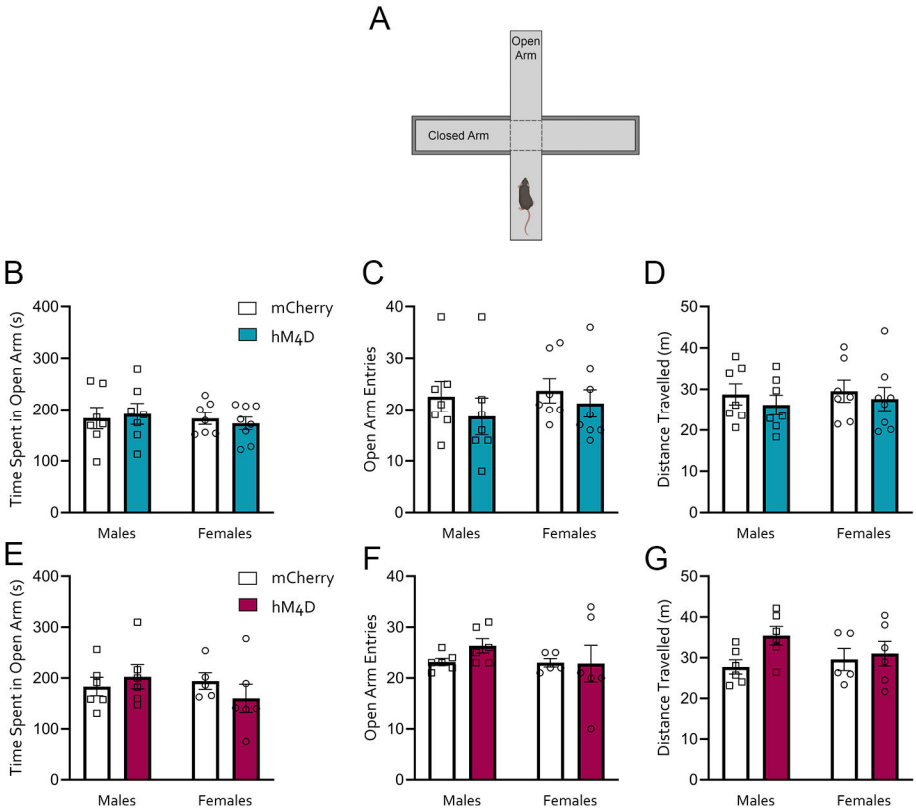

Figure S5. Chronic inhibition of the vCA1-mPFC pathway does not affect long-term performance in the elevated plus maze. A. Following the experiments from Figure 7, animals in both the juvenile and adult cohorts were tested in the elevated plus maze (EPM) in the absence of C21. **B-D**. Juvenile cohort. mCherry and hM4D animals

944 that underwent C21 treatment from P15-P30 did not differ in time spent in the open
945 arms of the EPM (**B**; one-way ANOVA $F_{3, 25}$ = 0.2126, p =0.8867), number of open arm
946 entries (**C**; one-way ANOVA $F_{3, 25}$ = 0.5187, p =0.6733) or distance travelled (**D**; one-
947 way ANOVA $F_{3, 25}$ = 0.2966, p=0.8275). mCherry n= 14 (7 females, 7 males); hM4D n=
948 15 (8 females, 7 males). **E-G**. Adult cohort. mCherry and hM4D animals that underwent
949 C21 treatment from P60-P75 showed equivalent time spent in the open arms of the
950 EPM (**E**; one-way ANOVA $F_{3, 19}$ = 0.6785, p=0.5759), number of open arm entries (**F**;
951 one-way ANOVA $F_{3, 19}$ = 0.6532, p =0.5907) or distance travelled (**G**; one-way ANOVA
952 $F_{3, 19}$ = 1.807, p=0.1800). mCherry n= 11 (5 females, 6 males); hM4D n= 12 (6 females,
953 6 males). Individual female datapoints are represented as circles, and males as
954 squares.

955

956 **References:**

957 1. Eichenbaum, H. Hippocampus : Cognitive Processes and Neural Representations
958 that Underlie Declarative Memory The hippocampus serves a critical role in
959 declarative. *Neuron* **44**, 109–120 (2004).

960 2. O'Keefe, J. & Nadel, L. *The Hippocampus as a Cognitive Map*. *Hippocampus*
961 (1978).

962 3. Kheirbek, M. a *et al.* Differential control of learning and anxiety along the
963 dorsoventral axis of the dentate gyrus. *Neuron* **77**, 955–68 (2013).

964 4. Jimenez, J. C. *et al.* Anxiety Cells in a Hippocampal-Hypothalamic Circuit. *Neuron*
965 **97**, 670–683 (2018).

966 5. Gray, J. & Mcnaughton, N. *The Neuropsychology of Anxiety : An enquiry into the*
967 *function of the septo- hippocampal system Abstract and Keywords*. (2003).
968 doi:10.1093/acprof.

969 6. Fanselow, M. S. & Dong, H.-W. Are the dorsal and ventral hippocampus
970 functionally distinct structures? *Neuron* **65**, 7–19 (2010).

971 7. Besnard, A., Miller, S. M. & Sahay, A. Distinct Dorsal and Ventral Hippocampal
972 CA3 Outputs Govern Contextual Fear Discrimination. *Cell Rep.* **30**, 2360-2373.e5
973 (2020).

974 8. Sheehan, T. P., Chambers, R. A. & Russell, D. S. Regulation of affect by the
975 lateral septum: Implications for neuropsychiatry. *Brain Res. Rev.* **46**, 71–117
976 (2004).

977 9. AlSubaie, R. *et al.* Control of Parallel Hippocampal Output Pathways by
978 Amygdalar Long-Range Inhibition. *bioRxiv* 2021.03.08.434367 (2021).

979 10. Griffin, A. L. Role of the thalamic nucleus reunions in mediating interactions

980 between the hippocampus and medial prefrontal cortex during spatial working
981 memory. *Front. Syst. Neurosci.* **9**, 1–8 (2015).

982 11. Eichenbaum, H. Prefrontal–hippocampal interactions in episodic memory. *Nat.*
983 *Rev. Neurosci.* **18**, 547–558 (2017).

984 12. Jin, J. & Maren, S. Prefrontal-hippocampal interactions in memory and emotion.
985 *Front. Syst. Neurosci.* **9**, 1–8 (2015).

986 13. Sweeney, P. & Yang, Y. An inhibitory septum to lateral hypothalamus circuit that
987 suppresses feeding. *J. Neurosci.* **36**, 11185–11195 (2016).

988 14. Strange, B. a., Witter, M. P., Lein, E. S. & Moser, E. I. Functional organization of
989 the hippocampal longitudinal axis. *Nat. Rev. Neurosci.* **15**, 655–669 (2014).

990 15. Amaral, D. G. & Witter, M. P. The three-dimensional organization of the
991 hippocampal formation: a review of anatomical data. *Neuroscience* **31**, 571–591
992 (1989).

993 16. Moser, M. B. & Moser, E. I. Functional differentiation in the hippocampus.
994 *Hippocampus* **8**, 608–619 (1998).

995 17. Cembrowski, M. S. *et al.* Spatial Gene-Expression Gradients Underlie Prominent
996 Heterogeneity of CA1 Pyramidal Neurons. *Neuron* **89**, 351–368 (2016).

997 18. Thompson, C. L. *et al.* Genomic Anatomy of the Hippocampus. *Neuron* **60**, 1010–
998 1021 (2008).

999 19. Malik, R., Dougherty, K. A., Parikh, K., Byrne, C. & Johnston, D. Mapping the
1000 Electrophysiological and Morphological Properties of CA1 Pyramidal Neurons
1001 Along the Longitudinal Hippocampal Axis. **361**, 341–361 (2016).

1002 20. Jinno, S., Aika, Y., Fukuda, T. & Kosaka, T. Quantitative Analysis of Neuronal
1003 Nitric Oxide Synthase-Immunoreactive Neurons in the Mouse Hippocampus With
1004 Optical Disector. **412**, 398–412 (1999).

1005 21. Milior, G. *et al.* Electrophysiological Properties of CA1 Pyramidal Neurons along
1006 the Longitudinal Axis of the Mouse Hippocampus. *Nat. Publ. Gr.* 1–9 (2016)
1007 doi:10.1038/srep38242.

1008 22. Dong, H. W., Swanson, L. W., Chen, L., Fanselow, M. S. & Toga, A. W. Genomic-
1009 anatomic evidence for distinct functional domains in hippocampal field CA1. *Proc.*
1010 *Natl. Acad. Sci. U. S. A.* **106**, 11794–11799 (2009).

1011 23. Fanselow, M. S. & Dong, H. W. Are the Dorsal and Ventral Hippocampus
1012 Functionally Distinct Structures? *Neuron* (2010)
1013 doi:10.1016/j.neuron.2009.11.031.

1014 24. Biane, J. S. *et al.* Neural dynamics underlying associative learning in the dorsal
1015 and ventral hippocampus. *Nat. Neurosci.* **26**, 798–809 (2023).

1016 25. Jarzebowski, P., Hay, Y. A., Grewe, B. F. & Paulsen, O. Different encoding of
1017 reward location in dorsal and intermediate hippocampus. *Curr. Biol.* **32**, 834-
1018 841.e5 (2022).

1019 26. Barker, G. R. I. *et al.* Separate elements of episodic memory subserved by
1020 distinct hippocampal – prefrontal connections. *Nat. Neurosci.* **20**, (2017).

1021 27. Kheirbek, M. A. *et al.* Differential control of learning and anxiety along the
1022 dorsoventral axis of the dentate gyrus. *Neuron* **77**, 955–968 (2013).

1023 28. Bannerman, D. M. *et al.* Regional dissociations within the hippocampus - Memory
1024 and anxiety. *Neuroscience and Biobehavioral Reviews* (2004)
1025 doi:10.1016/j.neubiorev.2004.03.004.

1026 29. Bast, T., Wilson, L. A., Witter, M. P. & Morris, R. G. M. From rapid place learning
1027 to behavioral performance: A key role for the intermediate hippocampus. *PLoS*
1028 *Biol.* **7**, 0730–0746 (2009).

1029 30. Barker, G. R. I. *et al.* Separate elements of episodic memory subserved by
1030 distinct hippocampal-prefrontal connections. *Nat. Neurosci.* **20**, 242–250 (2017).

1031 31. O'Reilly, K. C. *et al.* Identification of dorsal–ventral hippocampal differentiation in
1032 neonatal rats. *Brain Struct. Funct.* **220**, 2873–2893 (2015).

1033 32. Lee, A. R., Kim, J. H., Cho, E., Kim, M. & Park, M. Dorsal and ventral
1034 hippocampus differentiate in functional pathways and differentially associate with
1035 neurological disease-related genes during postnatal development. *Front. Mol.*
1036 *Neurosci.* **10**, 1–14 (2017).

1037 33. Giedd, J. Structural magnetic resonance imaging of the adolescent brain. *Ann N Y*
1038 *Acad Sci.* **1021**, 77–85 (2004).

1039 34. Benes, F. M., Taylor, J. B. & Cunningham, M. C. Convergence and plasticity of
1040 monoaminergic systems in the medial prefrontal cortex during the postnatal
1041 period: implications for the development of psychopathology. *Cereb. Cortex* **10**,
1042 1014–27 (2000).

1043 35. Gogtay, N. *et al.* Dynamic mapping of human cortical development during
1044 childhood through early adulthood. *Proc. Natl. Acad. Sci. U. S. A.* **101**, 8174–9
1045 (2004).

1046 36. Paus, T., Keshavan, M. & Giedd, J. N. Why do many psychiatric disorders
1047 emerge during adolescence? *Nat. Rev. Neurosci.* **9**, 947–57 (2008).

1048 37. Van Eden, C. G., Kros, J. M. & Uylings, H. B. M. The development of the rat

1049 prefrontal cortex Its size and development of connections with thalamus , spinal
1050 cord and other cortical areas. *Prog. Brain Res.* **85**, 169–183 (1990).

1051 38. Andersen, S. L., Thompson, a T., Rutstein, M., Hostetter, J. C. & Teicher, M. H.
1052 Dopamine receptor pruning in prefrontal cortex during the periadolescent period in
1053 rats. *Synapse* **37**, 167–9 (2000).

1054 39. Kalsbeek, A., Voorn, P., Buijs, R. M., Pool, C. W. & Uylings, H. B. Development of
1055 the dopaminergic innervation in the prefrontal cortex of the rat. *J. Comp. Neurol.*
1056 **269**, 58–72 (1988).

1057 40. Lewis, D., Cruz, D., Eggan, S. & Erickson, S. Postnatal development of prefrontal
1058 inhibitory circuits and the pathophysiology of cognitive dysfunction in
1059 schizophrenia. *Ann N Y Acad Sci.* **1021**, 64–76 (2004).

1060 41. Brummelte, S., Witte, V. & Teuchert-Noodt, G. Postnatal development of GABA
1061 and calbindin cells and fibers in the prefrontal cortex and basolateral amygdala of
1062 gerbils (Meriones unguiculatus). *Int. J. Dev. Neurosci.* **25**, 191–200 (2007).

1063 42. Benes, F. M. & Farol, P. Myelination of a key relay zone in the hippocampal
1064 formation occurs in the human brain during childhood, adolescence, and
1065 adulthood. *Arch Gen Psychiatry* **51**, 477–84 (1994).

1066 43. Ming, G.-L. & Song, H. Adult neurogenesis in the mammalian brain: significant
1067 answers and significant questions. *Neuron* **70**, 687–702 (2011).

1068 44. Nadel, L. Some implications of postnatal hippocampal development.
1069 *Hippocampus* 1–10 (2021) doi:10.1002/hipo.23369.

1070 45. Li, L., Gao, X. & Zhou, Q. Neurobiology of Learning and Memory Absence of fear
1071 renewal and functional connections between prefrontal cortex and hippocampus
1072 in infant mice. *Neurobiol. Learn. Mem.* **152**, 1–9 (2018).

1073 46. Donato, F. *et al.* The Ontogeny of Hippocampus-Dependent Memories. **41**, 920–
1074 926 (2021).

1075 47. Cruz-Sanchez, A. *et al.* Developmental onset distinguishes three types of
1076 spontaneous recognition memory in mice. *Sci. Rep.* **10**, 1–11 (2020).

1077 48. Klune, C. B., Jin, B. & DeNardo, L. A. Linking mPFC circuit maturation to the
1078 developmental regulation of emotional memory and cognitive flexibility. *Elife* **10**,
1079 (2021).

1080 49. Chini, M. & Hanganu-Opatz, I. L. Prefrontal Cortex Development in Health and
1081 Disease: Lessons from Rodents and Humans. *Trends Neurosci.* **44**, 227–240
1082 (2021).

1083 50. Nabel, E. M. & Morishita, H. Regulating critical period plasticity: insight from the

1084 visual system to fear circuitry for therapeutic interventions. *Front. psychiatry* **4**,
1085 146 (2013).

1086 51. Giedd, J. N., Keshavan, M. & Paus, T. Why do many psychiatric disorders
1087 emerge during adolescence? *Nat rev neuroscie* **9**, 947–957 (2008).

1088 52. Lee, F. S. *et al.* Adolescent mental health— Opportunity and obligation. *Science*
1089 *(80-.).* **346**, 547–549 (2014).

1090 53. Casey, B. J., Glatt, C. E. & Lee, F. S. Treating the Developing versus Developed
1091 Brain: Translating Preclinical Mouse and Human Studies. *Neuron* **86**, 1358–1368
1092 (2015).

1093 54. Manoach, D. S. Prefrontal cortex dysfunction during working memory
1094 performance in schizophrenia: reconciling discrepant findings. *Schizophr. Res.*
1095 **60**, 285–298 (2003).

1096 55. Berman, K. F. & Weinberger, D. R. The prefrontal cortex in schizophrenia and
1097 other neuropsychiatric diseases : in vivo physiological correlates of cognitive
1098 deficits. *Prog. Brain Res.* **85**, 521–537 (1990).

1099 56. Meyer-Lindenberg, A. S. *et al.* Regionally specific disturbance of dorsolateral
1100 prefrontal-hippocampal functional connectivity in schizophrenia. *Arch. Gen.*
1101 *Psychiatry* **62**, 379–386 (2005).

1102 57. Wolf, R. C. *et al.* Temporally anticorrelated brain networks during working memory
1103 performance reveal aberrant prefrontal and hippocampal connectivity in patients
1104 with schizophrenia. *Prog. Neuro-Psychopharmacology Biol. Psychiatry* **33**, 1464–
1105 1473 (2009).

1106 58. Sigurdsson, T., Stark, K. L., Karayiorgou, M., Gogos, J. A. & Gordon, J. A.
1107 Impaired hippocampal-prefrontal synchrony in a genetic mouse model of
1108 schizophrenia. *Nature* **464**, 763–767 (2010).

1109 59. Bogerts, B. Recent advances in defining the neuropathology of schizophrenia.
1110 *Acta Neuropathol.* **19**, 431–445 (1993).

1111 60. MacMaster, F. P. & Kusumakar, V. Hippocampal volume in early onset
1112 depression. *BMC Med.* **2**, 2 (2004).

1113 61. Rao, U. *et al.* Hippocampal changes associated with early-life adversity and
1114 vulnerability to depression. *Biol. Psychiatry* **67**, 357–64 (2010).

1115 62. Sigurdsson, T. & Duvarci, S. Hippocampal-Prefrontal Interactions in Cognition ,
1116 Behavior and Psychiatric Disease. **9**, 1–18 (2016).

1117 63. Li, M., Long, C. & Yang, L. Hippocampal-prefrontal circuit and disrupted functional
1118 connectivity in psychiatric and neurodegenerative disorders. *Biomed Res. Int.*

1119 **2015**, (2015).

1120 64. Hartung, H. *et al.* From Shortage to Surge: A Developmental Switch in
1121 Hippocampal-Prefrontal Coupling in a Gene-Environment Model of
1122 Neuropsychiatric Disorders. *Cereb. Cortex* **26**, 4265–4281 (2016).

1123 65. Oberlander, V. C., Xu, X., Chini, M. & Hanganu-Opatz, I. L. Developmental
1124 dysfunction of prefrontal–hippocampal networks in mouse models of mental
1125 illness. *Eur. J. Neurosci.* **50**, 3072–3084 (2019).

1126 66. Xu, X., Song, L. & Hanganu-Opatz, I. L. Knock-Down of Hippocampal DISC1 in
1127 Immune-Challenged Mice Impairs the Prefrontal-Hippocampal Coupling and the
1128 Cognitive Performance throughout Development. *Cereb. Cortex* **31**, 1240–1258
1129 (2021).

1130 67. Barón-Mendoza, I. *et al.* Dendritic complexity in prefrontal cortex and
1131 hippocampus of the autistic-like mice C58/J. *Neurosci. Lett.* **703**, 149–155 (2019).

1132 68. Adams, R. A. *et al.* Impaired theta phase coupling underlies frontotemporal
1133 dysconnectivity in schizophrenia. *Brain* **143**, 1261–1277 (2020).

1134 69. Zerbi, V. *et al.* Dysfunctional autism risk genes cause circuit-specific connectivity
1135 deficits with distinct developmental trajectories. *Cereb. Cortex* **28**, 2495–2506
1136 (2018).

1137 70. Tamura, M., Mukai, J., Gordon, J. A. & Gogos, J. A. Developmental Inhibition of
1138 Gsk3 Rescues Behavioral and Neurophysiological Deficits in a Mouse Model of
1139 Schizophrenia Predisposition. *Neuron* **89**, 1100–1109 (2016).

1140 71. Cenquizca, L. a & Swanson, L. W. Spatial organization of direct hippocampal field
1141 CA1 axonal projections to the rest of the cerebral cortex. *Brain Res. Rev.* **56**, 1–
1142 26 (2007).

1143 72. Ahlbeck, J., Song, L., Chini, M., Bitzenhofer, S. H. & Hanganu-Opatz, I. L.
1144 Glutamatergic drive along the septotemporal axis of hippocampus boosts
1145 prelimbic oscillations in the neonatal mouse. *Elife* **7**, 1–24 (2018).

1146 73. Takita, M., Fujiwara, S. E. & Izaki, Y. Functional structure of the intermediate and
1147 ventral hippocampo-prefrontal pathway in the prefrontal convergent system. *J.*
1148 *Physiol. Paris* **107**, 441–447 (2013).

1149 74. Little, J. P. & Carter, A. G. Subcellular Synaptic Connectivity of Layer 2 Pyramidal
1150 Neurons in the Medial Prefrontal Cortex. *J. Neurosci.* **32**, 12808–12819 (2012).

1151 75. Liu, X. & Carter, A. G. Ventral Hippocampal Inputs Preferentially Drive
1152 Corticocortical Neurons in the Infralimbic Prefrontal Cortex. **38**, 7351–7363
1153 (2018).

1154 76. Hallock, H. L. *et al.* Molecularly-Defined Hippocampal Inputs Regulate Population
1155 Dynamics in the Prelimbic Cortex to Suppress Context Fear Memory Retrieval.
1156 *Biol. Psychiatry* 802967 (2020) doi:10.1016/j.biopsych.2020.04.014.

1157 77. Lee, A. T. *et al.* VIP Interneurons Contribute to Avoidance Behavior by Regulating
1158 Information Flow across Hippocampal-Prefrontal Networks. *Neuron* **102**, 1223-
1159 1234.e4 (2019).

1160 78. Schlichting, M. L., Preston, A. R., States, U., States, U. & States, U. HHS Public
1161 Access. 1–8 (2016) doi:10.1016/j.cobeha.2014.07.005.Memory.

1162 79. Sánchez-Bellot, C., AlSubaie, R., Mishchanchuk, K., Wee, R. W. S. & MacAskill,
1163 A. F. Two opposing hippocampus to prefrontal cortex pathways for the control of
1164 approach and avoidance behaviour. *Nat. Commun.* **13**, 1–17 (2022).

1165 80. Williams, S. A. *et al.* Hippocampal Disinhibition Reduces Contextual and
1166 Elemental Fear Conditioning While Sparing the Acquisition of Latent Inhibition.
1167 *eNeuro* **9**, 1–14 (2022).

1168 81. Labouesse, M. A., Langhans, W. & Meyer, U. Abnormal context–reward
1169 associations in an immune-mediated neurodevelopmental mouse model with
1170 relevance to schizophrenia. *Transl. Psychiatry* **5**, 1–9 (2015).

1171 82. Hensch, T. K. Critical period regulation. *Annu. Rev. Neurosci.* **27**, 549–79 (2004).

1172 83. Fox, K. A Critical Period for Experience-dependent Barrel Cortex Synaptic
1173 Plasticity in Rat. *J. Neurosci.* **12**, 1626–1636 (1992).

1174 84. Fagiolini, M., Pizzorusso, T., Berardi, N., Domenici, L. & Maffei, L. Functional
1175 postnatal development of the rat primary visual cortex and the role of visual
1176 experience: dark rearing and monocular deprivation. *Vision Res.* **34**, 709–20
1177 (1994).

1178 85. Gordon, A. & Sttyker, P. Experience-Dependent Primary Visual Cortex Plasticity
1179 of Binocular of the Mouse Responses in the. **76**, 3274–3286 (1996).

1180 86. Travaglia, A., Steinmetz, A. B., Miranda, J. M. & Alberini, C. M. Mechanisms of
1181 critical period in the hippocampus underlie object location learning and memory in
1182 infant rats. *Learn. Mem.* **25**, 176–182 (2018).

1183 87. Alberini, C. M. & Travaglia, A. Infantile Amnesia: A Critical Period of Learning to
1184 Learn and Remember. *J. Neurosci.* **37**, 5783–5795 (2017).

1185 88. Ramsaran, A. I., Schlichting, M. L. & Frankland, P. W. The ontogeny of memory
1186 persistence and specificity. *Dev. Cogn. Neurosci.* **36**, 100591 (2019).

1187 89. Thomases, D. R., Cass, D. K. & Tseng, K. Y. Periadolescent exposure to the
1188 NMDA receptor antagonist MK-801 impairs the functional maturation of local

1189 GABAergic circuits in the adult prefrontal cortex. *J. Neurosci.* **33**, 26–34 (2013).

1190 90. Rebello, T. J. *et al.* Postnatal Day 2 to 11 Constitutes a 5-HT-Sensitive Period
1191 Impacting Adult mPFC Function. *J. Neurosci.* **34**, 12379–12393 (2014).

1192 91. Callaghan, B. L., Graham, B. M., Li, S. & Richardson, R. From resilience to
1193 vulnerability: mechanistic insights into the effects of stress on transitions in critical
1194 period plasticity. *Front. psychiatry* **4**, 90 (2013).

1195 92. Espinosa, J. S. & Stryker, M. P. Development and plasticity of the primary visual
1196 cortex. *Neuron* **75**, 230–49 (2012).

1197 93. Hubel, D. & Wiesel, T. THE PERIOD OF SUSCEPTIBILITY TO THE
1198 PHYSIOLOGICAL EFFECTS OF UNILATERAL EYE CLOSURE IN KITTENS. *J.*
1199 *Physiol.* **206**, 419–436 (1970).

1200 94. Erzurumlu, R. S. & Gaspar, P. Development and critical period plasticity of the
1201 barrel cortex. *Eur. J. Neurosci.* **35**, 1540–53 (2012).

1202 95. Perica, M. I. & Luna, B. Impact of stress on excitatory and inhibitory markers of
1203 adolescent cognitive critical period plasticity. *Neurosci. Biobehav. Rev.* **153**,
1204 (2023).

1205 96. Yang, X. D. *et al.* Stress during a Critical Postnatal Period Induces Region-
1206 Specific Structural Abnormalities and Dysfunction of the Prefrontal Cortex via
1207 CRF 1. *Neuropsychopharmacology* **40**, 1203–1215 (2015).

1208 97. Dajani, D. R. & Uddin, L. Q. Demystifying cognitive flexibility: Implications for
1209 clinical and developmental neuroscience. *Trends Neurosci.* **38**, 571–578 (2015).

1210 98. Armbruster, D. J. N., Ueltzhöffer, K., Basten, U. & Fiebach, C. J. Prefrontal
1211 cortical mechanisms underlying individual differences in cognitive flexibility and
1212 stability. *J. Cogn. Neurosci.* **24**, 2385–2399 (2012).

1213 99. Gläscher, J. *et al.* Lesion mapping of cognitive control and value-based decision
1214 making in the prefrontal cortex. *Proc. Natl. Acad. Sci. U. S. A.* **109**, 14681–14686
1215 (2012).

1216 100. Durstewitz, D., Vittoz, N. M., Floresco, S. B. & Seamans, J. K. Abrupt transitions
1217 between prefrontal neural ensemble states accompany behavioral transitions
1218 during rule learning. *Neuron* **66**, 438–448 (2010).

1219 101. Milner, B. Effects of Different Brain Lesions on Card Sorting. *Arch Neurol* **9**, 90–
1220 100 (1963).

1221 102. AM, O., Roberts, A., CE, P., BJ, S. & Robbins, T. Extra-dimensional versus intra-
1222 dimensional set shifting performance following frontal lobe excisions, temporal
1223 lobe excisions or amygdalo-hippocampectomy in man. *Neuropsychologia* **29**,

1224 993–1006 (1991).

1225 103. Dias, R., Robbins, T. W. & Roberts, A. C. Dissociable forms of inhibitory control
1226 within prefrontal cortex with an analog of the wisconsin card sort test: Restriction
1227 to novel situations and independence from 'on-line' processing. *J. Neurosci.* **17**,
1228 9285–9297 (1997).

1229 104. Dias, R., Robbins, T. W. & Roberts, A. C. Dissociation in prefrontal cortex of
1230 affective and attentional shifts. *Nature* **380**, 69–72 (1996).

1231 105. Canetta, S. E. *et al.* Mature parvalbumin interneuron function in prefrontal cortex
1232 requires activity during a postnatal sensitive period. *Elife* **11**, 1–24 (2022).

1233 106. Benoit, L. J. *et al.* Adolescent thalamic inhibition leads to long-lasting impairments
1234 in prefrontal cortex function. *Nat. Neurosci.* **25**, 714–725 (2022).

1235 107. Jett, J. D., Bulin, S. E., Hatherall, L. C., McCartney, C. M. & Morilak, D. A. Deficits
1236 in cognitive flexibility induced by chronic unpredictable stress are associated with
1237 impaired glutamate neurotransmission in the rat medial prefrontal cortex.
1238 *Neuroscience* **346**, 284–297 (2017).

1239 108. Birrell, J. M. & Brown, V. J. Medial frontal cortex mediates perceptual attentional
1240 set shifting in the rat. *J. Neurosci.* **20**, 4320–4324 (2000).

1241 109. Brooks, J. M. *et al.* Transient inactivation of the neonatal ventral hippocampus
1242 impairs attentional set-shifting behavior: Reversal with an α7 nicotinic agonist.
1243 *Neuropsychopharmacology* **37**, 2476–2486 (2012).

1244 110. Marquis, J. P., Goulet, S. & Doré, F. Y. Neonatal ventral hippocampus lesions
1245 disrupt extra-dimensional shift and alter dendritic spine density in the medial
1246 prefrontal cortex of juvenile rats. *Neurobiol. Learn. Mem.* **90**, 339–346 (2008).

1247 111. Godsil, B. P., Kiss, J. P., Spedding, M. & Jay, T. M. The hippocampal-prefrontal
1248 pathway: The weak link in psychiatric disorders? *Eur. Neuropsychopharmacol.*
1249 (2013) doi:10.1016/j.euroneuro.2012.10.018.

1250 112. Ghoshal, A. & Conn, P. J. The hippocampo-prefrontal pathway: a possible
1251 therapeutic target for negative and cognitive symptoms of schizophrenia. *Futur.*
1252 *Neurol* **10**, 115–128 (2015).

1253 113. Brockmann, M. D., Pöschel, B., Cichon, N. & Hanganu-Opatz, I. L. Coupled
1254 Oscillations Mediate Directed Interactions between Prefrontal Cortex and
1255 Hippocampus of the Neonatal Rat. *Neuron* **71**, 332–347 (2011).

1256 114. Xu, X., Chini, M., Bitzenhofer, S. H. & Hanganu-Opatz, I. L. Transient knock-down
1257 of prefrontal DISC1 in immune-challenged mice causes abnormal long-range
1258 coupling and cognitive dysfunction throughout development. *J. Neurosci.* **39**,
1259 1222–1235 (2019).

1260 115. Arruda-carvalho, M., Wu, W., Cummings, K. A. & Clem, R. L. Optogenetic
1261 Examination of Prefrontal-Amygdala Synaptic Development. *J. Neurosci.* **37**,
1262 2976–2985 (2017).

1263 116. Britt, J. P. *et al.* Synaptic and Behavioral Profile of Multiple Glutamatergic Inputs
1264 to the Nucleus Accumbens. *Neuron* **76**, 790–803 (2012).

1265 117. LeGates, T. A. *et al.* Reward behaviour is regulated by the strength of
1266 hippocampus–nucleus accumbens synapses. *Nature* **564**, 258–262 (2018).

1267 118. Bagot, R. C. *et al.* Ventral hippocampal afferents to the nucleus accumbens
1268 regulate susceptibility to depression. *Nat. Commun.* **6**, 7062 (2015).

1269 119. Parfitt, G. M. *et al.* Bidirectional Control of Anxiety-Related Behaviors in Mice:
1270 Role of Inputs Arising from the Ventral Hippocampus to the Lateral Septum and
1271 Medial Prefrontal Cortex. *Neuropsychopharmacology* **42**, 1715–1728 (2017).

1272 120. Glangetas, C. *et al.* NMDA-receptor-dependent plasticity in the bed nucleus of the
1273 stria terminalis triggers long-term anxiolysis. *Nat. Commun.* **8**, (2017).

1274 121. Xu, C. *et al.* Distinct Hippocampal Pathways Mediate Dissociable Roles of
1275 Context in Memory Retrieval. *Cell* **167**, 961-972.e16 (2016).

1276 122. Dolleman-Van Der Weel, M. J. *et al.* The nucleus reuniens of the thalamus sits at
1277 the nexus of a hippocampus and medial prefrontal cortex circuit enabling memory
1278 and behavior. *Learn. Mem.* **26**, 191–205 (2019).

1279 123. Ciocchi, S., Passecker, J., Mikus, N. & Klausberger, T. Selective information
1280 routing by ventral hippocampal CA1 projection neurons. **348**, (2015).

1281 124. Padilla-Coreano, N. *et al.* Direct Ventral Hippocampal-Prefrontal Input Is Required
1282 for Anxiety-Related Neural Activity and Behavior. *Neuron* **89**, 857–866 (2016).

1283 125. Adhikari, A., Topiwala, M. a & Gordon, J. a. Synchronized activity between the
1284 ventral hippocampus and the medial prefrontal cortex during anxiety. *Neuron* **65**,
1285 257–69 (2010).

1286 126. Kishi, T., Tsumori, T., Yokota, S. & Yasui, Y. Topographical projection from the
1287 hippocampal formation to the amygdala: a combined anterograde and retrograde
1288 tracing study in the rat. *J. Comp. Neurol.* **496**, 349–68 (2006).

1289 127. Kim, W. Bin & Cho, J. H. Synaptic targeting of double-projecting ventral CA1
1290 hippocampal neurons to the medial prefrontal cortex and basal amygdala. *J.*
1291 *Neurosci.* **37**, 4868–4882 (2017).

1292 128. Hoover, W. B. & Vertes, R. P. Anatomical analysis of afferent projections to the
1293 medial prefrontal cortex in the rat. *Brain Struct. Funct.* **212**, 149–179 (2007).

1294 129. Moser, M. & Moser, E. I. Distributed Encoding and Retrieval of Spatial Memory in
1295 the Hippocampus. **18**, 7535–7542 (1998).

1296 130. Dong, H. W. & Swanson, L. W. Projections from bed nuclei of the stria terminalis,
1297 anteromedial area: Cerebral hemisphere integration of neuroendocrine,
1298 autonomic, and behavioral aspects of energy balance. *J. Comp. Neurol.* **494**,
1299 142–178 (2006).

1300 131. Rizzi-Wise, C. A. & Wang, D. V. Putting together pieces of the lateral septum:
1301 Multifaceted functions and its neural pathways. *eNeuro* **8**, (2021).

1302 132. Ye, X., Kapeller-Libermann, D., Travaglia, A., Inda, M. C. & Alberini, C. M. Direct
1303 dorsal hippocampal-prelimbic cortex connections strengthen fear memories. *Nat.*
1304 *Neurosci.* **20**, 52–61 (2017).

1305 133. Spear, L. P. *The adolescent brain and age-related behavioral manifestations.*
1306 *Neuroscience and biobehavioral reviews* vol. 24 (2000).

1307 134. Reincke, S. A. J. & Hanganu-opatz, I. L. Early-life stress impairs recognition
1308 memory and perturbs the functional maturation of prefrontal- hippocampal-
1309 perirhinal networks. *Sci. Rep.* 1–16 (2017) doi:10.1038/srep42042.

1310 135. Wang, H. X. & Gao, W. J. Cell type-specific development of NMDA receptors in
1311 the interneurons of rat prefrontal cortex. *Neuropsychopharmacology* **34**, 2028–
1312 2040 (2009).

1313 136. Kirkwood, A., Lee, H. & Bear, M. Co-regulation of long-term potentiation and
1314 experience-dependent synaptic plasticity in visual cortex by age and experience.
1315 *Nature* **375**, 328–31 (1995).

1316 137. Antonini, a, Fagiolini, M. & Stryker, M. P. Anatomical correlates of functional
1317 plasticity in mouse visual cortex. *J. Neurosci.* **19**, 4388–406 (1999).

1318 138. Antonini, A. & Stryker, M. P. Rapid Remodeling of Axonal Arbors in the Visual
1319 Cortex. *Science (80-.).* **260**, 1819–1821 (1993).

1320 139. Holtmaat, A. J. G. D. *et al.* Transient and persistent dendritic spines in the
1321 neocortex in vivo. *Neuron* **45**, 279–291 (2005).

1322 140. Zuo, Y., Lin, A., Chang, P. & Gan, W. B. Development of long-term dendritic spine
1323 stability in diverse regions of cerebral cortex. *Neuron* **46**, 181–189 (2005).

1324 141. Botterill, J. J., Gerencer, K. J., Vinod, K. Y., Alcantara-Gonzalez, D. & Scharfman,
1325 H. E. Dorsal and ventral mossy cells differ in their axonal projections throughout
1326 the dentate gyrus of the mouse hippocampus. *Hippocampus* **31**, 522–539 (2021).

1327 142. Botterill, J. J. *et al.* Dorsal peduncular cortex activity modulates affective behavior
1328 and fear extinction in mice. *Neuropsychopharmacology* 1–14 (2024)

1329 doi:10.1038/s41386-024-01795-5.

1330 143. Linke, R., Pabst, T. & Frotscher, M. Development of the hippocamposeptal
1331 projection in the rat. *J. Comp. Neurol.* **351**, 602–616 (1995).

1332 144. Tsamis, K. I., Lagartos Donato, M. J., Dahl, A. G., O'Reilly, K. C. & Witter, M. P.
1333 Development and topographic organization of subicular projections to lateral
1334 septum in the rat brain. *Eur. J. Neurosci.* **52**, 3140–3159 (2020).

1335 145. Zhang, Z. wei. Maturation of Layer V Pyramidal Neurons in the Rat Prefrontal
1336 Cortex: Intrinsic Properties and Synaptic Function. *J. Neurophysiol.* **91**, 1171–
1337 1182 (2004).

1338 146. Kroon, T., van Hugte, E., van Linge, L., Mansvelder, H. D. & Meredith, R. M. Early
1339 postnatal development of pyramidal neurons across layers of the mouse medial
1340 prefrontal cortex. *Sci. Rep.* **9**, 1–16 (2019).

1341 147. Reynolds, L. M. & Flores, C. Mesocorticolimbic Dopamine Pathways Across
1342 Adolescence: Diversity in Development. *Front. Neural Circuits* **15**, 1–17 (2021).

1343 148. Reynolds, L. M. *et al.* DCC Receptors Drive Prefrontal Cortex Maturation by
1344 Determining Dopamine Axon Targeting in Adolescence. *Biol. Psychiatry* 1–12
1345 (2017) doi:10.1016/j.biopsych.2017.06.009.

1346 149. Hoops, D., Reynolds, L. M. & Flores, C. Dopamine Development in the Mouse
1347 Orbital Prefrontal Cortex Is Protracted and Sensitive to Amphetamine in
1348 Adolescence. **5**, 1–9 (2018).

1349 150. Reynolds, L. M. *et al.* Early Adolescence is a Critical Period for the Maturation of
1350 Inhibitory Behavior. *Cereb. Cortex* **29**, 3676–3686 (2019).

1351 151. Gergues, M. M. *et al.* Circuit and molecular architecture of a ventral hippocampal
1352 network. *Nat. Neurosci.* **23**, 1444–1452 (2020).

1353 152. Ueda, S. *et al.* Sequence of Molecular Events during the Maturation of the
1354 Developing Mouse Prefrontal Cortex. *Complex Psychiatry* **1**, 94–104 (2015).

1355 153. Miyamae, T., Chen, K., Lewis, D. A. & Gonzalez-Burgos, G. Distinct physiological
1356 maturation of parvalbumin-positive neuron subtypes in mouse prefrontal cortex. *J.*
1357 *Neurosci.* **37**, 4883–4902 (2017).

1358 154. Yang, J. M., Zhang, J., Yu, Y. Q., Duan, S. & Li, X. M. Postnatal development of 2
1359 microcircuits involving fast-spiking interneurons in the mouse prefrontal cortex.
1360 *Cereb. Cortex* **24**, 98–109 (2014).

1361 155. Canetta, S. *et al.* Mature parvalbumin interneuron function in prefrontal cortex
1362 requires activity during a postnatal sensitive period. *bioRxiv* 7031–7031 (2022)
1363 doi:10.1007/978-3-319-19650-3_304535.

1364 156. Brockmann, M. D., Pöschel, B., Cichon, N. & Hanganu-Opatz, I. L. Coupled
1365 oscillations mediate directed interactions between prefrontal cortex and
1366 hippocampus of the neonatal rat. *Neuron* **71**, 332–47 (2011).

1367 157. Song, L. *et al.* Sparser and Less Efficient Hippocampal-Prefrontal Projections
1368 account for Developmental Network Dysfunction in a Model of Psychiatric Risk
1369 Mediated by Gene-Environment Interaction. *J. Neurosci.* **42**, 601–618 (2022).

1370 158. Parent, M. A., Wang, L., Su, J., Netoff, T. & Yuan, L. L. Identification of the
1371 hippocampal input to medial prefrontal cortex in vitro. *Cereb. Cortex* **20**, 393–403
1372 (2010).

1373 159. Jay, T. M., Glowinski, J. & Thierry, A. M. Selectivity of the hippocampal projection
1374 to the prelimbic area of the prefrontal cortex in the rat. *Brain Res.* **505**, 337–340
1375 (1989).

1376 160. Liu, X., Dimidschstein, J., Fishell, G. & Carter, A. G. Hippocampal inputs engage
1377 cck+ interneurons to mediate endocannabinoid-modulated feed-forward inhibition
1378 in the prefrontal cortex. *Elife* **9**, 1–22 (2020).

1379 161. Zhang, Z. Maturation of Layer V Pyramidal Neurons in the Rat Prefrontal Cortex :
1380 Intrinsic Properties and Synaptic Function. *J. Neurophysiol.* **91**, 1171–1182
1381 (2004).

1382 162. Cizeron, M. *et al.* A brainwide atlas of synapses across the mouse life span.
1383 *Science (80-.).* **369**, 270–275 (2020).

1384 163. Bolles, R. C. & Woods, P. J. The ontogeny of behaviour in the albino rat. *Anim.*
1385 *Behav.* **12**, 427–441 (1964).

1386 164. Sellinger, E. P., Drzewiecki, C. M., Willing, J. & Juraska, J. M. Cell death in the
1387 male and female rat medial prefrontal cortex during early postnatal development.
1388 *IBRO Neurosci. Reports* **10**, 186–190 (2021).

1389 165. Premachandran, H., Zhao, M. & Arruda-Carvalho, M. Sex Differences in the
1390 Development of the Rodent Corticolimbic System. *Front. Neurosci.* **14**, (2020).

1391 166. Brenhouse, H. C. & Andersen, S. L. Developmental trajectories during
1392 adolescence in males and females: a cross-species understanding of underlying
1393 brain changes. *Neurosci. Biobehav. Rev.* **35**, 1687–703 (2011).

1394 167. Walker, D. M. *et al.* Adolescence and Reward : Making Sense of Neural and
1395 Behavioral Changes Amid the Chaos. **37**, 10855–10866 (2017).

1396 168. Koss, W. a, Belden, C. E., Hristov, A. D. & Juraska, J. M. Dendritic remodeling in
1397 the adolescent medial prefrontal cortex and the basolateral amygdala of male and
1398 female rats. *Synapse* **68**, 61–72 (2014).

169. Derks, N. A. V., Krugers, H. J., Hoogenraad, C. C., Joëls, M. & Angela Sarabdjitsingh, R. Effects of early life stress on synaptic plasticity in the developing hippocampus of male and female rats. *PLoS One* **11**, 1–17 (2016).

170. Zitman, F. M. & Richter-Levin, G. Age and sex-dependent differences in activity, plasticity and response to stress in the dentate gyrus. *Neuroscience* **249**, 21–30 (2013).

171. Rabiant, K., Antol, J., Naassila, M. & Pierrefiche, O. Sex difference in the vulnerability to hippocampus plasticity impairment after binge-like ethanol exposure in adolescent rat: Is estrogen the key? *Addict. Biol.* **26**, 1–12 (2021).

172. Page, C. E. & Coutellier, L. Adolescent Stress Disrupts the Maturation of Anxiety-related Behaviors and Alters the Developmental Trajectory of the Prefrontal Cortex in a Sex- and Age-specific Manner. *Neuroscience* **390**, 265–277 (2018).

173. Bueno-Fernandez, C. *et al.* Long term effects of peripubertal stress on excitatory and inhibitory circuits in the prefrontal cortex of male and female mice. *Neurobiol. Stress* **14**, (2021).

174. Urban, K. R. & Valentino, R. J. Age- And sex-dependent impact of repeated social stress on intrinsic and synaptic excitability of the rat prefrontal cortex. *Cereb. Cortex* **27**, 244–253 (2017).

175. Wei, J. *et al.* Estrogen protects against the detrimental effects of repeated stress on glutamatergic transmission and cognition. *Mol. Psychiatry* **19**, 588–598 (2014).

176. Juraska, J. M. & Willing, J. Pubertal onset as a critical transition for neural development and cognition. *Brain Res.* **1654**, 87–94 (2017).

177. Willing, J., Drzewiecki, C. M., Cuenod, B. A., Cortes, L. R. & Juraska, J. M. A role for puberty in water maze performance in male and female rats. *Behav. Neurosci.* **130**, 422–427 (2016).

178. Piekarski, D. J., Boivin, J. R. & Wilbrecht, L. Ovarian Hormones Organize the Maturation of Inhibitory Neurotransmission in the Frontal Cortex at Puberty Onset in Female Mice. *Curr. Biol.* **27**, 1735–1745 (2017).

179. Piekarski, D. J. *et al.* Does puberty mark a transition in sensitive periods for plasticity in the associative neocortex ? *Brain Res.* **1654**, 123–144 (2017).

180. Griffiths, B. B., Madden, A. M. K., Edwards, K. A., Zup, S. L. & Stary, C. M. Age-dependent sexual dimorphism in hippocampal cornu ammonis-1 perineuronal net expression in rats. *Brain Behav.* **9**, 1–5 (2019).

181. Drzewiecki, C. M., Willing, J. & Juraska, J. M. Influences of age and pubertal status on number and intensity of perineuronal nets in the rat medial prefrontal cortex. *Brain Struct. Funct.* **225**, 2495–2507 (2020).

1435 182. Hensch, T. K. Critical period mechanisms in developing visual cortex. *Curr. Top.*
1436 *Dev. Biol.* **69**, 215–37 (2005).

1437 183. Hensch, T. K. Local GABA Circuit Control of Experience-Dependent Plasticity in
1438 Developing Visual Cortex. *Science (80-.).* **282**, 1504–1508 (1998).

1439 184. Iwai, Y., Fagiolini, M., Obata, K. & Hensch, T. K. Rapid critical period induction by
1440 tonic inhibition in visual cortex. *J. Neurosci.* **23**, 6695–702 (2003).

1441 185. Premachandran, H., Wilkin, J. & Arruda-carvalho, M. Minimizing Variability in
1442 Developmental Fear Studies in Mice : Toward Improved Replicability in The Field.
1443 1–25 (2024) doi:10.1002/cpz1.1040.

1444 186. Canetta, S. *et al.* Differential Synaptic Dynamics and Circuit Connectivity of
1445 Hippocampal and Thalamic Inputs to the Prefrontal Cortex. *Cereb. Cortex*
1446 *Commun.* **1**, 1–15 (2020).

1447 187. Pöpplau, J. A. *et al.* Reorganization of adolescent prefrontal cortex circuitry is
1448 required for mouse cognitive maturation. *Neuron* **112**, 421-440.e7 (2024).

1449 188. Reynolds, L. M. *et al.* Amphetamine disrupts dopamine axon growth in
1450 adolescence by a sex-specific mechanism in mice. *Nat. Commun.* **14**, (2023).

1451 189. Bitzenhofer, S. H., Pöpplau, J. A., Chini, M., Marquardt, A. & Hanganu-Opatz, I. L.
1452 A transient developmental increase in prefrontal activity alters network maturation
1453 and causes cognitive dysfunction in adult mice. *Neuron* **109**, 1350-1364.e6
1454 (2021).

1455 190. Morgan, A. A. *et al.* Medial Prefrontal Cortex Serotonin Input Regulates Cognitive
1456 Flexibility in Mice. *bioRxiv* **6216**, 1–34 (2023).

1457 191. Franklin, K. B. J. & Paxinos, G. *The Mouse Brain in Stereotaxic Coordinates*
1458 *(map)*. *Academic Press* (2007).

1459 192. Dong, H., Swanson, L. W., Chen, L., Fanselow, M. S. & Toga, A. W. Genomic –
1460 anatomic evidence for distinct functional domains in hippocampal field CA1. **106**,
1461 (2009).

1462 193. Arruda-Carvalho, M. & Clem, R. L. Pathway-selective adjustment of prefrontal-
1463 amygdala transmission during fear encoding. *J. Neurosci.* **34**, 15601–15609
1464 (2014).

1465 194. Cruikshank, S. J., Urabe, H., Nurmikko, A. V & Connors, B. W. Pathway-specific
1466 feedforward circuits between thalamus and neocortex revealed by selective
1467 optical stimulation of axons. *Neuron* **65**, 230–45 (2010).

1468